Journal of Inorganic and Organometallic Polymers and Materials (2022) 32:4320–4339
https://doi.org/10.1007/s10904-022-02448-0

Unravelling the Synthetic Mimic, Spectroscopic Insights, and Supramolecular Crystal Engineering of an Innovative Heteronuclear Pb(II)-Salen Cocrystal: An Integrated DFT, QTAIM/NCI Plot, NLO, Molecular Docking/PLIP, and Antibacterial Appraisal

Dhrubajyoti Majumdar[1,2] · Jessica Elizabeth Philip[3] · Burak Tüzün[4] · A. Frontera[5] · Rosa M. Gomila[5] · Sourav Roy[6] · Kalipada Bankura[1]

Received: 22 May 2022 / Accepted: 5 July 2022 / Published online: 26 July 2022
© The Author(s), under exclusive licence to Springer Science+Business Media, LLC, part of Springer Nature 2022

Abstract

Spontaneous self-assembly in the supramolecular entity is one of the enthralling synthetic routes. It produces disparate structure crystal complexes after selecting suitable M-L combinations in the pseudohalide sense. In this attempt, a novel cocrystal is synthesized from two independent components (0D + 1D), $[PbCd(L^1)(SCN)_2]\cdot[PbCd(L^1)(SCN)_2]_n$ **(1)** using a Salen (H_2L^1) and NaSCN, which was characterized by spectroscopic, EDX, SEM, PXRD, and X-ray crystallography. The title complex crystallizes in the triclinic space group *P1* with unit cell parameters: a = 8.5733(2), b = 11.3798(2), c = 27.105(5) Å, V = 2583.95(9) $Å^3$, and Z = 4. X-ray structure divulges the de-protonated form of $[L^{-2}]$, comprising Cd(II)/Pb(II) ions placed in the inner N_2O_2 and outer O_4 compartments. The Cd(II)/Pb(II) metal ions satisfy trigonal-prismatic and square pyramidal geometries. Crystal engineering and Hirshfeld surface approaches delineate the dominant interactions, e.g., H-bonding (36.4%), C···H (20.8%), and S···H (21.1%). The unique chalcogen (ChB)/tetrel bonds observed in its solid-state architecture were authenticated by DFT using the PBo-D3/def2-TZVP level of theory. The QTAIM/NCI plot reveals the nature of these contacts. The S···S distance is 2.499(4) Å, and the C–S···S angle is close to linearity (168.8°), confirming the typical ChB. The MEP surface explores the most nucleophilic part at the N-atom belonging to the bonding of Cd-NCS (– 42 kcal/mol). HOMO–LUMO energy gap and NLO parameters provide chemical reactivity and sensitive optical information about the molecules. Meanwhile, Molecular docking was conceded based on total energy with three bacterial proteins like Staphylococcus aureus (PDB ID: 1JIJ) and pseudomonas aeruginosa (PDB ID: 3JPU), and Escherichia coli (PDB ID: 5MMN). Docking and PLIP confirmed the bioactivity of the complex. The compound was screened in vitro against two-gram + ve and

✉ Dhrubajyoti Majumdar
dmajumdar30@gmail.com

1 Department of Chemistry, Tamralipta Mahavidyalaya, Tamluk 721636, West Bengal, India

2 Department of Chemistry and Chemical Biology, Indian Institute of Technology (Indian School of Mines), Dhanbad, Jharkhand 826004, India

3 Department of Chemistry, Deva Matha College, Kuravilangadu, Kottayam 686633, Kerala, India

4 Department of Plant and Animal Production, Sivas Vocational School, Sivas Cumhuriyet University, TR-58140 Sivas, Turkey

5 Department de Quimica, Universitat de Les Illes Balears, Cra. de Valldemossa km 7.5, 07122 Palma de Mallorca, (Baleares), Spain

6 Solid State and Structural Chemistry Unit, Indian Institute of Science, Bangalore 560 012, India

two-gram -ve bacteria. The complex had lower MIC (µg/mL) values (10.1) compared to the parent ligand (32.7), implying greater antimicrobial efficiencies. The time-kill kinetics led to the bactericidal activities of the complex.

Graphical abstract

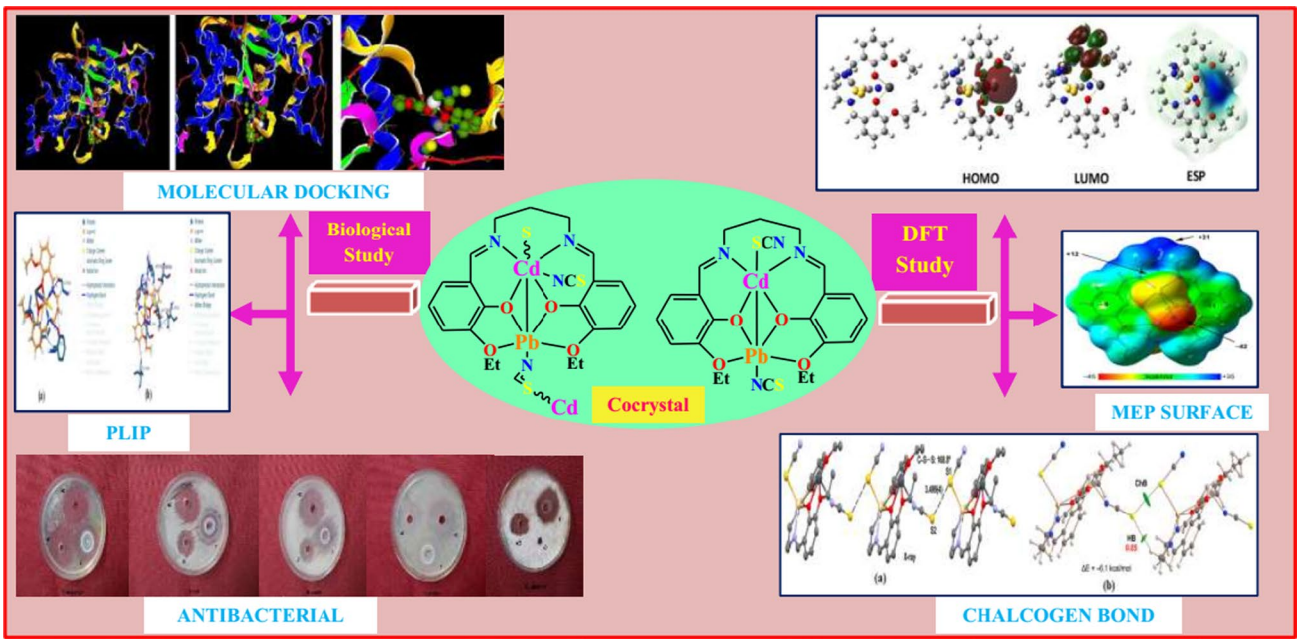

Keywords Antimicrobial · Cocrystal · DFT · Molecular docking · PLIP · Salen ligand

1 Introduction

Over the last few years, the coordination chemistry of the Salen ligand has amplified the multidimensional research if we concentrate our attention on the cocrystal concept [1]. Cocrystal formation is one of the most cardinal solid-state research projects due to its versatile applications like antimicrobial, catalyst, photosystem II, magnetic, and metal enzymes [2]. Contemporary, a new research direction is envisaged in various fields concerning advanced crystalline materials, e.g., human life improvement and environmental rehabilitation [3–8]. Although cocrystals mostly captivate the attention in organic and pharmaceutical research, few metal complexes are cumbersome [9–11]. Therefore, today the isolation and characterization of various cocrystals are one of the most active research areas in a modern solid-state environment [12–20]. The term cocrystal defines the formation of multi-component crystals [21]. It allows fine-tuning solubility, dissolution, and bioavailability without changing their molecular structure [1]. It is noteworthy that the rational design and successful synthesis of cocrystals is a challenging task [21–28] since they have comparable crystallization kinetics and the lattice packing forces for different coordinate geometries, structures, and shapes [29]. There is also the right choice of ligand, solvent, temperature, and maintenance of the stoichiometric and enantiomeric ratios [30]. Interestingly, cocrystals in metal complexes are (a) Metal–ligand hybrid systems with different structures; (b) metal complexes with non-coordinated ligands; (c) special additives with metal complexes [30]. In addition, the term cocrystals have been known for a long time [2]. The first reported normal cocrystal, quinhydrone. It consists of quinone and hydroquinone, first described by Wohler as late as the nineteenth century [31]. The first cocrystals of Schiff bases, in which a metal atom is also present in the crystal structure, were reported in 2008 [32, 33]. The research on cocrystal applications has only emerged in decades. Co-crystallization of Salen with other bioactive molecules and their coordination with metal ions are often biologically relevant. This orientation inspired coordination chemists to conduct further research on Salen cocrystals, especially in crystal engineering, NLO activities, and biological activities associated with DFT-based experiments Molecular docking (MD)/Protein–ligand interaction profiler (PLIP). Herein crystal engineering is fascinating for searching for any supramolecular interactions present. The Molecular docking and PLIP research support the cocrystal drug-like properties [34–40]. Furthermore, the coordination chemistry of Pb(II) is not sacred, and any homo/hetero cocrystal

complexes of Pb to date are reported in the literature in the presence of thiocyanate linkers (Scheme S1) [41, 42]. We focused on synthesizing Pb(II)-cocrystal to dig into supramolecular architectures formed by non-covalent interactions and Chalcogen/Tetrel/spodium/σ-hole bonds [43–49]. The synthesized complex configuration is comparable to those observed in other Cd(II) complexes prepared with ligand H_2L^1 [50] or analog one bearing methoxy groups instead of ethoxy [51–53]. The high atomic number (Z = 82) and the radius were sufficient to encompass other coordination numbers from 2 to 10 to proceed in variable valence states of Pb, which attracted synthetic inorganic chemists to map unique lead complexes [41, 54–57]. Most Pb materials are trained in semiconductors, batteries, ferroelectrics, and nonlinear optics [37, 58–62]. The polarizable Pb(II) is particularly interested in forming tetrel bonds between these Group IV elements. Pb(II) can act as an electron donor to trap supramolecular interactions. Pb(II) can arise thanks to a Hemi-directed coordination environment and a stereochemically active lone pair $6s^2$, [63] leading to a significant coordination gap. The tetrel bond [64, 65] is generally characterized by two different structural organizations, namely: Holo/Hemi-directed (Scheme S2) [66–68]. However, always little research has explored the Tetrel-bonded in the lead cocrystals [69–72].

In this endeavour, the present work highlights the synthetic mimics, spectroscopic characterization, and X-ray structure of one privileged Pb(II)-Salen cocrystal. Hirshfeld's surface successfully substantiates the crystal packing of supramolecular interactions. DFT validated the chalcogen/tetrel bonds and the QTAIM/NCI Plot, further disclosing the nature of these contacts. The NLO parameters support the optical behaviour. The global chemical parameters like the HOMO–LUMO energy gap further ensure compound reactivity. The antibacterial efficacy and time-kill kinetics also accomplish the cocrystal compound. Overtone's concept fruitfully explains the main reason for the antibacterial action on the complex over the Salen. MD and PLIP experiments have observed an excellent biological tie-up with the interaction between metal complex and bacterial proteins based on total energy against the reference molecule streptomycin.

2 Experimental

2.1 Materials and Instrumentation

In the current research, all reagents and solvents were purchased from Aldrich, Sigma, USA, or Merck Chemical Company and were used without further purification. The solvents like Methanol and Acetonitrile (ACN) were of spectroscopic quality. Elemental analyses (C, H, and N) were performed using a PerkinElmer 2400 CHN Elemental Analyzer. IR/Raman spectra were recorded as KBr pellets (4000–400 cm^{-1}). It uses a PerkinElmer Spectrum like RX 1 and BRUKER RFS 27 (4000–50 cm^{-1}) model. $^1H/^{13}C$-NMR spectra were collected on a Bruker 400 MHz and 75.45 MHz FT NMR spectrometer using TMS in DMSO-d6 standard. BRUKER AXS performed PXRD measurements and the GERMANY X-ray diffractometer D8 FOCUS model with Cu K-α radiation. UV–Visible spectra of the Salen and the cocrystal complex (200–1100 nm) were determined using the Hitachi model U-3501 spectrophotometer.

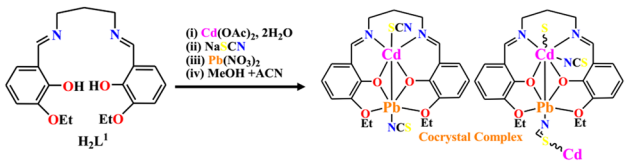

Scheme 1 Outline the synthetic scheme for the cocrystal complex

2.2 Synthesis of Salen ligand ($H_2L.^1$)

Salen ligand was synthesized using the previously reported popular literature method (Scheme1) [42]. In brief, ligand is the 1:2 condensation product of 1,3-diaminopropane (0.037 g, 0.5 mmol) with 3-ethoxy-2-hydroxybenzaldehyde (0.166 g, 1 mmol) in (50 mL) methanol at 75 °C for 1 h. The yellow-coloured Salen ligand separated upon cooling the solution. It was collected and dried. N,N'-Bis(3-methoxysalicylidenimino)-1,3-diaminoproane (H_2L^1): Yield: (90%), Anal. Calc. for $C_{21}H_{26}N_2O_4$: C, 68.09; H, 7.07; N, 7.56 Found: C, 68.07; H, 7.11; N, 7.60%. IR (KBr cm^{-1}) selected bands: ν(C=N), 1632, $\nu(C\text{-}O_{phenolic})$1252, ^1H NMR (DMSO-d6, 400 MHz): δ (ppm): 2.51 ($2H^9$), 3.69 ($2H^8$), 6.87–7.45 (m, $1H^3$-$1H^5$), 8.59 (m, $1H^6$), 13.53 (Phenolic-OH), ^{13}C NMR (DMSO-d6, 75.45 MHz): δ (ppm): 56.41 ($O\text{-}CH_2CH_3$), 116.92–132.75 (Arom-C), 161.15 (C–OH), 166.66 (CH = N), UV–Vis λ_{max} (CH_3OH): 338 nm.

2.3 Synthesis of $[PbCd(L^1)(SCN)_2]\cdot[PbCd(L.^1)(SCN)_2]_n$ (1)

$Cd(OAc)_2.2H_2O$ (0.219 g, 1 mmol) and the Salen ligand (0.359 g, 1 mmol) were dissolved after heating in 30 mL methanol, followed by drop-wise addition of an aqueous methanolic solution (5 mL) of NaSCN (0.081 g, 1 mmol). The overall solution was stirred for 1 h under a magnetic stirrer. In the meantime, we added ten drops of hot methanol solution of $Pb(NO_3)_2$ (0.331 g, 1 mmol). Then the resultant mixture was refluxed at room temperature for 2 h. Finally, pour six drops of acetonitrile (ACN) into this refluxed solution. The light-yellow solution was filtered and stored

refrigerated for crystallization by slow evaporation. After several days of spending, block-sized, yellow-coloured single crystals were obtained, suitable for SCXRD. Crystals were isolated by filtration and air-dried. Yield: 0.430 g, (58%), Anal. Calc. for $C_{23}H_{24}CdN_4O_4PbS_2$: C, 34.35; H, 3.01; N, 6.97. Found: C, 34.31; H, 3.06; N, 7.03%. FT-IR (KBr cm^{-1}) selected bands: ν(C=N), 1623 S, ν(NCS), 2088s, ν(SCN), 2160 m, ν(Ar–O),1406 s, FT-Raman (cm^{-1}) selected bands: ν(C=N), 1620 s, ν(NCS), 2095s, ν(SCN), 2152 m, ^{1}H NMR (DMSO-d6, 400 MHz): δ (ppm): 1.85 (s, $3H^1$), 3.78 (m, $2H^2$), 2.51 (m, $2H^9$), 3.41 (m, $2H^8$), 6.41–7.10 (m, $1H^3$-$1H^5$), 8.15–8.31 (w, $1H^6$), (Scheme S5), UV–Vis λ_{max} (DMF): 357 nm.

2.4 X-ray Crystallography

Yellow cocrystal complexes were grown upon slow evaporation of the mixed solvent of methanol and acetonitrile medium after spending several days. We selected 3–4 good quality crystals with microscopic observation for crystal data processing purposes. Crystal was collected on a Bruker CCD [73] diffractometer using Mo Kα radiation at room temperature (λ = 0.71073 Å). For data collection, we used several crystallographic programs. *SMART* is used for accumulating information frames, indexing reflections, and determining lattice parameters, *SAINT* [74] for combining the intensity of reflections and scaling, *SADAB* [75] for absorption correction, and *SHELXTL* for space group and structure determination, and least-squares refinements on *F2*. The crystal structure was solved by full-matrix least-squares methods against *F2* using *SHELXL*-2014 [76] and *Olex-2* software [77]. All non-H atoms were refined with anisotropic shift parameters, and all hydrogen positions were constant at calculated positions, resulting in sensitive isotropic. A summary of crystallographic information and complete structure refinement parameters are shown in Table 1.

Table 1 Crystal data and structure refinement parameters

Formula	$C_{23}H_{24}CdN_4O_4PbS_2$
M/g	804.178
Crystal system	Triclinic
Space group	*P* 1
a/Å	8.5733(2)
b/Å	11.3798(2)
c/Å	27.105(5)
α (°)	88.274(10)
β (°)	89.366(10)
γ(°)	77.846(10)
V/Å^3	2583.95(9)
Colour	Yellow
Z	4
ρ_c/gcm^{-3}	2.067
μ/mm^{-1}	7.528
F (000)	1536
Cryst size (mm^3)	0.086 × 0.066 × 0.044
θ range (deg)	0.75 to 28.04
Limiting indices	− 11 ≤ h ≤ 11
	− 15 ≤ k ≤ 12
	− 35 ≤ l ≤ 35
Reflns collected	40346
Ind reflns	12364 [R_{int} = 0.0554, *R*sigma = 0.0673]
Completeness to *θ* (%)	0.998
Refinement method	Full-matrix-block least-squares on F^2
Data/restraints/ parameters	12364/0/623
Goodness-of-fit on F^2	1.035
Final *R* indices [$I > 2\sigma(I)$]	R_1 = 0.0435
	wR_2 = 0.0834
R indices (all data)	R_1 = 0.0739
	wR_2 = 0.0962
Largest diff. peak and hole(e·Å^{-3})	1.757 and − 1.504

2.5 DFT Methodology

In connection with the complex, we utilized two different levels of theory for DFT calculation. The first calculations reported herein were performed using the Gaussian-16 program [78]. For the analysis, we used crystallographic coordinates of the complex using the PBo-D3/def2-TZVP level of theory [79, 80]. The basis set includes cadmium and lead metals' effective core potentials (ECP). It takes into consideration relativistic effects for the inner electrons [81]. Such a level of theory has been used to evaluate noncovalent interactions in the solid-state [82, 83]. The MEP surface plot was obtained using the wavefunction obtained at the same level of theory. Herein the 0.01 a. u. iso-surface to simulate the van der Waals envelope. The topological electron density was calculated using QTAIM and the NCI plot. These two were proposed by Bader [84] and W. Yang et al. [85], respectively. Both were represented using the AIM all program [86] and using the following settings for the NCI plot index representation: s = 0.5 a. u.; cut-off ρ = 0.04 a. u., and color scale – 0.04 ≤ sign (λ2)ρ ≤ 0.04 a. u. The second DFT calculations provide essential information about the molecules' chemical and biological properties [87–90]. The calculated parameters are vividly used to explain the chemical activities of the molecules. The theoretical calculations were made on the B3LYP, Hf, and M062x levels [91–93] in the Lanl2dz and SDD basis set using the Gaussian package program [86] Gaussian09 RevD.01 and Gauss View 6.0 [94, 95]. Using DFT, many quanta chemical parameters have been found, describing the different chemical properties of the molecules. These parameters are HOMO (Highest

Occupied Molecular Orbital), LUMO (Lowest Unoccupied Molecular Orbital), and ΔE (HOMO–LUMO energy gap). Also, the chemical potential (μ), electrophilicity (ω), chemical hardness (η), global softness (σ), dipole moment, the energy value is calculated [96, 97].

$$\chi = -\left(\frac{\partial \mathrm{E}}{\partial \mathrm{N}}\right)_{v(r)} = \frac{1}{2}(I + A) \cong -\frac{1}{2}(E_{HOMO} + E_{LUMO})$$

$$\eta = -\left(\frac{\partial^2 \mathrm{E}}{\partial \mathrm{N}^2}\right)_{v(r)} = \frac{1}{2}(I - A) \cong -\frac{1}{2}(E_{HOMO} - E_{LUMO})$$

$$\sigma = 1/\eta\omega = \chi^2/2\eta\varepsilon = 1/\omega$$

Further, the biological activities of the complex against cancer proteins were compared. The proteins and metal complex files were studied at HEX 8.0.0 programs [98]. The antibacterial calculations against the crystal structures of Staphylococcus aureus protein (PDB ID: 1JIJ), Pseudomonas aeruginosa protein (PDB ID: 3JPU), [99] and Escherichia coli protein (PDB ID: 5MMN) [100] were performed. The following parameters are used for docking: correlation type shape only, FFT mode: 3D, grid dimension: 0.6, receptor range: 180, ligand range: 180, twist range: 360, distance range: 40. Finally, the Protein–Ligand Interaction Profiler (PLIP) server confirmed the interaction between protein and the metal complex [101].

2.6 Experimental of Antimicrobial

2.6.1 Bacterial Cultures

The synthesized cocrystals were tested for their in vitro antibacterial using the Agar Well Diffusion method (for the qualitative determination). For the said purpose, four sensitive microorganisms used are *Staphylococcus aureus* (ATCC 25,923) and *Bacillus subtilis* (ATCC 6635) as Gram-positive bacteria. The other *Pseudomonas aeruginosa* (ATCC 27,853), and *Escherichia coli* (ATCC 25,922) as Gram-negative bacteria. The serial dilutions in liquid broth method for determination of MIC values. Importantly, all ATCC strains were procured from the American Type Culture Collection (ATCC, Manassas, VA, USA). The media used in the study were purchased from Hi-Media, India.

2.6.2 Maintenance of Cultures

The preservation of all the bacterial cultures predominantly in 50% glycerol at -70 °C (vol/vol; Hi-Media, Mumbai, India). Primarily maintained it on Trypticase Soy Agar (TSA; Difco Laboratories, Detroit, Mich USA).

2.6.3 In Vitro Antimicrobial Study

The crystal sample was inoculated with *Staphylococcus aureus*, *Bacillus subtilis, Pseudomonas aeruginosa,* and *Escherichia coli* and incubated at 37 °C. The microbial turbidity was adjusted equivalent to a 0.5 McFarland turbidity standard. After that, Mueller–Hinton agar plates (Merck, 105,437) were swabbed uniformly with the standardized inoculums. Again, once dried, the agar plates' surfaces, 6 mm three wells, were bored using a sterile cork-borer about two cm apart. Each well of the bottom was coated with sterilized Mueller–Hinton agar at 45 °C. The sample was dissolved in DMSO for each microorganism, then added into one of the wells, and allowed to diffuse at room temperature for 2 h. It loaded DMSO as negative control (− C) and streptomycin (+ C) for bacterial culture. All the plates were incubated face upwards among bacterial cultures incubated at 37 °C for 24–48 h. The diameter of the inhibition zones was evaluated using a microscope scale, and six replications were maintained for each plate. Data were analyzed by ANOVA using the Origin pro 8.5 statistical software, and the mean differences were separated using Tukey's studentized test at the 1% probability level.

2.6.4 Time Kill Kinetic

The time-kill kinetics studies of the synthesized compound were conducted against all the selected microbes. This experiment uses an overnight culture of the isolates 1 mL of 10^6 CFU mL^{-1} of each culture. It was inoculated in sterilized nutrient broth media containing 25 $mgmL^{-1}$ of the compounds and was conducted for 13 h in a shaker at 30 °C. Likewise, prepared control for each microorganism without having the test compound. It is necessary to take CFU count at a regular one-hour interval.1 mL of each culture was spread on nutrient agar plates from 0 to 13 h. Each dish was incubated for 24 h at 30 °C. The CFU (colony forming unit) was calculated and plotted.

2.6.5 Determination of MIC-Agar Dilution Method

An essential method like agar dilution involves the incorporation of varying desired concentrations of the antimicrobial agent into an agar medium (molten agar medium). It habitually uses serial two-fold dilutions. It was then injected a defined microbial inoculum onto the agar plate surface. The MIC endpoint is recorded as the lowest concentration of antimicrobial agent that completely inhibits growth under suitable incubation conditions. This technique is ideal for antibacterial susceptibility testing.

3 Results and Discussion

3.1 Synthetic Mimics

The synthetic mimics of the coordination chemistry researcher is an open platform to explore the novel crystal complex formations. The title cocrystal was synthesized as ongoing research on Schiff base metal complexes. It aimed to prepare and investigate novel properties of heterometallic cocrystal compounds. The popular Salen ligand was synthesized using the previous literature method (Scheme 1) [42]. The complex derived moderately good yield from cadmium acetate dihydrate and lead nitrate as metal precursors. In addition, the Salen ligand and the thiocyanate spacer in a 1:1:1:1 molar ratio used in situ self-assembly method (Scheme1). The complex is insoluble in water and sparingly soluble in most common organic solvents. We add Cd(II) and Pb(II) metal ions for the repeated synthetic procedure. In all cases, Cd(II) occupies the inner N_2O_2 and Pb(II) the outer O_4 cavities, probably due to the larger size of Pb(II), whose ionic radius (133 pm) is much larger than that of Cd(II) (109 pm) [37, 102]. It is noteworthy that single crystals were grown not only in methanol as the solvent. So, we used a few drops of acetonitrile to promote crystals with better diffraction quality suitable for SCXRD. Although this type of ligand is widely used to synthesize homo- and heteronuclear complexes, this (0D + 1D) cocrystal is unique. An overlook of the Salen includes two imines, two phenols, and two alkoxy groups. These donor centers always explore highly chelating coordination behaviour. After deprotonation, the reference Salen always generates an N_2O_2-imine chelating position (Scheme S3–S4) [103]. The complex configuration is comparable to those observed in homonuclear cadmium complexes prepared with the ligand H_2L^1 or analog-bearing methoxy groups instead of ethoxy (L^{OMe}) [50–53]. This type of Salen has never been used to construct heteronuclear (0D + 1D) cocrystal complexes. Interestingly, most recent publications on heteronuclear lead complexes mainly explore DFT-based supramolecular crystal engineering. Herein the crystal engineering highlighted only the ChB/tetrel bonding along with the Hemi-/holo-directed nature of lead metal [102, 104–106]. Our ongoing research on the cocrystal complex delves into ChB/tetrel bonding and bactericidal activity based on the collaboration with MD/PLIP experiments. Both experiments substantiate the synthesized compound is bioactive. Further, in this article, the enhanced antibacterial activity of the complex over the ligand is explained by Overtone's and Tweedy's chelation concept. We also explore the complex time-kill kinetics study, which exhibits basic pharmacodynamic information on the relationship between the compound and the growth of microorganisms. Therefore, we ensure synthetic mimicking of unique heteronuclear cocrystal formation using the popular Salen is an exciting research effort.

3.2 Spectroscopic Characterization

The structural characterization of as-synthesized compounds is an integral part of coordination chemistry research. Therefore, we used FTIR/Raman/NMR spectroscopy to characterize Salen, the title compound, and the bridging propensity of SCN^- ions. The ligand's identified imine (C = N) stretching near 1632 cm^{-1} (Fig.S1) [107]. In the complex, the stretching bands for IR/Raman (C = N) are shifted to 1623 cm^{-1} (Fig.S2) and 1620 cm-1 (Fig.S3). These data support the coordination of the azomethine nitrogen atom to the Cd metal centre [108]. Further, thiocyanate spacers (SCN-) displayed two strong bifurcated bands in 2088, 2160 cm^{-1} (**1**) (IR) and 2095, 2152 cm^{-1} (**1**) (Raman). These splitting patterns are attributed to two distinct binding modes with the Cd and Pb metal ions [109]. The UV–Visible absorption spectra of the ligand and the compound were analyzed in CH_3OH and DMF to ensure the electronic transitions. Ligands exhibit bands at 338 nm (Fig.S4) for $\pi \rightarrow \pi^*/n \rightarrow \pi^*$ type transitions. In contrast, the complex reveals a potent ligand-based UV domain at 357 nm (Fig.S5) due to the $L \rightarrow M$ charge-transfer transition ($\pi \rightarrow \pi^*/n \rightarrow \pi^*$) [108, 110]. All the spectral data mentioned above are identical to the previously reported Salen [111, 112]. Due to the filled d^{10} configuration and the diamagnetic nature of cadmium metal ion, no metal-centered broad d-d absorption band has been identified. The Free Salen ligand in the region δ 5.0–8.0 ppm did not show a broad peak, indicating the absence of the $-NH_2$ group. The NMR peak value at δ 3.69 ppm identified the H^8 aliphatic proton. The phenolic protons (OH^7) are associated with the defined broad peak at δ 13.53 ppm. The protons (H^6) attached to the imino carbon are downfield shifted δ 8.15–8.31 ppm [80, 81] due to the influence of the combined effect of phenolic -OH and imino N groups in its close vicinity. The peaks at δ 6.41–7.10 ppm correspond to the aromatic protons ($1H^3$-$1H^5$), whereas the three methyl protons ($OCH_2CH^1{}_3$) attached to the aromatic oxygen appear at δ 1.85 ppm (Fig.S6). The azomethine-N coordination mode was assigned to the downfield shift of the azomethine proton signal from the ligand. The OH proton (OH^7) signal at the ligand disappeared in the ^1H NMR spectra of the complex (Fig.S8). It divulges deprotonation and coordination of the O-atom with Cd metal ions [111, 112]. The essential ^{13}C NMR spectra of the Salen showed the azomethine (CH = N) carbons at 166.66 ppm, 56.41 ($O\text{-}CH_2CH_3$), 116.92–132.75 (Arom-C), 161.15 (C–OH) ppm, respectively, (Fig.S7). All the spectral analyses confirm the Salen ligand and the complex configuration.

3.3 EDX and PXRD

EDX is an X-ray procedure. It is used to identify the elemental composition of complex materials. The generated EDX data consists of spectra showing peaks corresponding to the elements that make up the accurate composition of the analysed sample. Applying the EDX technique to the complex, we successfully identify the chemical composition of Cd and Pb as metal ions. Aside from that, C, O, S, and N as elemental compositions (Table S3 and Fig.S9). Thus, the empirical formula of the complex is fully justified. The EDX profile reflects the highest peak Pb, followed by Cd metal ions. The PXRD method further studied the phase purity and crystallinity, and recorded diffraction patterns were at room temperature. Experimentally scanning the compound in the range ($2\theta = 40–50^0$) recorded the PXRD patterns. The well-defined sharp PXRD peaks of the compound support the crystalline nature (Fig.S10A). The complex's experimental and simulated PXRD patterns match well, indicating the consistency of the bulk sample.

3.4 SEM Characterization

A scanning electron microscope (SEM) is an electron microscope system. It produces images of a sample by scanning the surface with a focused beam of electrons. The electrons interact with the sample atom and generate various signals containing information about the synthesized compound's surface topography, size, and morphological structure. We performed an SEM experiment with our cocrystal complex, and the different SEM images of the complex are shown in Fig.S10B. The SEM figures directly exhibited the morphology of distributed overlapping sheets, probably analogous to S. M. Sheta et al. published work [113].

4 Single-Crystal X-ray Diffraction

4.1 X-ray Crystal Structure

The X-ray single-crystal structure determination revealed that complex **1** crystallizes in the triclinic space group *P*-1 with Z = 4. The complex contains two independent heteronuclear units, A and B, with different geometries (0D + 1D) (Fig. 1a, b). Unit A is polymeric and includes repeating hetero di-nuclear neutral units of $[(SCN)Cd(L^1)Pb(NCS)]_n$, joined through a single end-to-end, thiocyanate bridge. The Cd(II) centers occupy the inner N_2O_2 core in each di-metallic unit. The Pb(II) centers reside in the outer O_4 body of the compartmental deprotonated Salen $[L^{2-}]$. The competitive occupation of Cd(II) vs. Pb(II) is another intriguing aspect of the stereochemistry observed in this cocrystal. Cd(II) occupies the inner N_2O_2, and Pb(II) occupies the outer O_4 compartments. The significant Pb(II) ionic radius (133 pm) is much larger than that of Cd(II) metal ions (109 pm). It is difficult for Pb(II) to be accommodated in the inner N_2O_2 compartment, where the Cd(II) fits well with the outer O_4 cavities. Therefore, Pb(II) ion delivers well in the open external O_4 pit [37, 102]. A perspective view of the polymeric unit A and B with the corresponding atom numbering scheme is given in Fig. 1a and b. All the selected bond parameters related are summarized in Table S1.

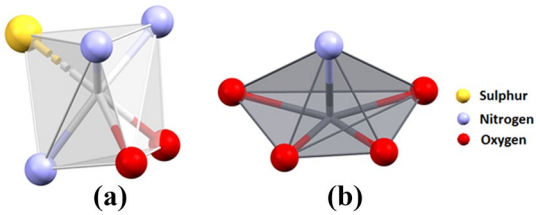

Fig. 2 Perspective view of **a** trigonal prismatic geometry of Cd(II) center, and **b** square pyramidal geometry of Pb(II) center in unit A

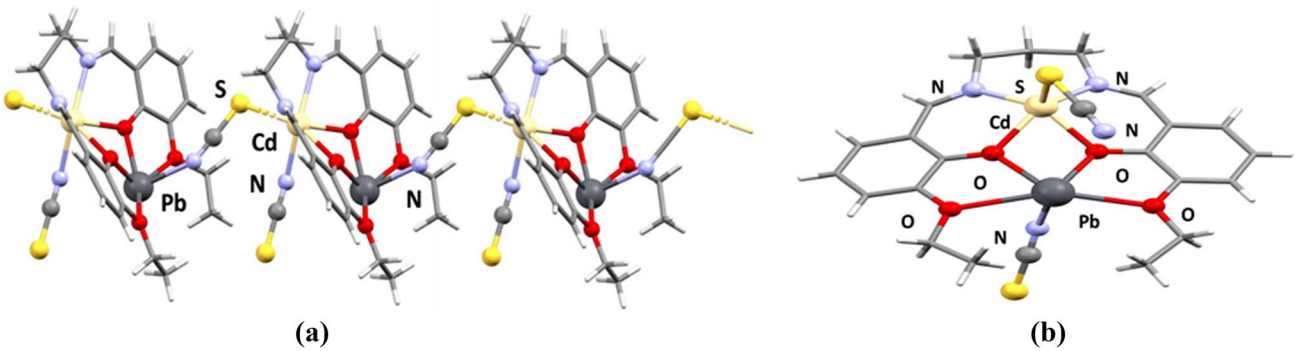

Fig. 1 Perspective view of complex **a** for unit A, and **b** for unit B with selective different atoms

The Cd(II) centers are hexacoordinated with trigonal prismatic geometries, whereas the Pb(II) centers are Penta-coordinated with square pyramidal geometries (Fig. 2a, b). Cd(2) is coordinated by two imine nitrogen atoms, N(6) and N(5), and two phenoxy oxygen atoms, O(7) and O(6), of the deprotonated [L^{2-}], constituting the equatorial plane. N(8), one nitrogen atom, occupies the fifth coordination site from a thiocyanate molecule. A Sulphur atom, S(3), from a symmetry-related (− 1 + x, y, z) end-to-end bridged thiocyanate occupies the sixth coordination site of Cd(II) to form a distorted trigonal prismatic geometry. Pb(2) is coordinated by four oxygen atoms constituting the basal plane. Among them, two are phenoxy oxygen atoms, [O(6) and O(7)], and the other two are ethoxy oxygen atoms, O(5) and O(5). The Pb–O(phenoxy) bond distances (~ 2.296 Å) are lesser compared to that of the Pb–O(ethoxy) bond distances (~ 2.691 Å). The 5th coordination position is occupied by a nitrogen atom, N(7), from a bridging thiocyanate at a distance of 2.431(7) Å, forming a square pyramidal geometry with significant distortion. The distortion from square pyramidal to trigonal bipyramid is calculated by the Addison parameter (τ) [114]. The τ value for the Pb(2) center is 0.31, indicating that the geometry is distorted square pyramidal. Cd(II) and Pb(II) center are bridged by two phenoxy oxygen atoms, O(7) and O(6), with a Cd(2)···Pb(2) distance of 3.504(5) Å. The bridging angles, Cd(2)–O(6)–Pb(2) and Cd(2)–O(7)–Pb(2), are 99.3(2)° and 98.6(2)°, respectively. The saturated six-membered chelate ring [Cd(2)–N(5)–C(33)–C(34)–C(35)–N(6)] has an envelope conformation with puckering parameters q = 0.630(7) Å, θ = 7.9(6)°, and ϕ = 227(4)° [115]. Similar envelope conformations have been observed in several metal Salen complexes [116]. It is worthy to note the orientation assumed by the SCN at cadmium with a C22-S1-Cd1 bond angle of 90.7(3) °. So that the terminal N3 results almost at the apex of the PbO_4 based at 3.398(10)Å from the metal, indicating a strong possible tetrel type bonding interaction. Such incidents are comparable to previously reported Pb complexes (Table S2).

Unit B (Fig. 1b) contains a hetero di-nuclear unit of [(SCN)Cd(L^1)Pb(NCS)], where both the metal centers [Cd(1) and Pb(1)] are Penta-coordinated. Cd(1) sits in the inner core of the ligand coordinated by two imine nitrogen atoms, [N(1) and N(2)] and two phenoxy oxygen atoms, [O(2) and O(3)]. The 5th site is coordinated by an S atom, S(1), from a thiocyanate molecule. Pb(1) sits in the outer core of the ligand coordinated by two phenoxy oxygen atoms, [O(2) and O(3)], and two ethoxy oxygens, [O(1) and O(4)]. The axial site is occupied by the nitrogen atom, N(4), from a thiocyanate molecule. The τ value[1] around Cd(1) and Pb(1) centers are 0.09 and 0.33, respectively, indicating that both geometries are square-pyramidal with an ample amount of distortion observed for the Pb(1) center. Cd(II) and Pb(II) centers are bridged by two phenoxy oxygen atoms, O(2) and O(3), with a Cd(1)···Pb(1) distance of 3.561(6) Å. The M–O(phenoxy) bond distances are lesser than that of the M–O(ethoxy) bond distances. The bridging angles, Cd(1)–O(2)–Pb(1) and Cd(1)–O(3)–Pb(1), are [102(2)° and 102.9(2)°, respectively] higher compared to that of unit A. The saturated six-membered chelate ring [Cd(1)–N(1)–C(10)–C(11)–C(12)–N(2)] has an envelope conformation with puckering parameters q = 0.458(7) Å, θ = 164.2(10)°, and ϕ = 180(4)° [115]. The Pearson theory holds very well for the thiocyanate modus operandi [30]. Between Cd(II) and Pb(II) ions, the former is a hard acid, and the latter is a soft acid. Thus, the S atom (soft base) of thiocyanate is preferably linked to the soft acid Pb(II), and the nitrogen atom (hard base) is related to the hard acid Cd(II) ion. Further studies of the Cambridge Structural Database (CSD) (Fig.S9) confirmed the preferred thiocyanate N-bonded bonding with d^{10} Cd(II) metal ions [41]. Although this ligand has been widely reported for synthesizing homo- and hetero di-nuclear complexes, the Cd/Pb cocrystal complex is unique. These geometric values and the complex configuration are comparable to those observed in homo di-nuclear Cd complexes prepared with the ligand (H_2L^1) or an analog with methoxy groups instead of ethoxy (L^{OMe}) [50–53]. The Pb–O structural parameters measured in Ni/Pb(L) [104] /Ni/Pb(L^{OMe}) [117] complexes (where Pb occupies the outer coordination sphere) agree with the reported data of the complex.

4.2 Crystal Packing and Supramolecular Interactions

Different non-covalent supramolecular interactions like H-bonding, C − H···π, π···π, C-H···π(SCN), C − H···H − C, are observed in the solid-state of the complex which governed the crystal packing (Fig. 3a) of the complex. Unit A itself is a polymer, but unit B is di-nuclear, which forms a zigzag supramolecular chain through C-H···π(SCN) interactions (Fig. 3a). In the crystal packing, it is observed that two A units are surrounded by two zigzag supramolecular chains of the B unit. Unit A forms C − H···H − C interactions within themselves, whereas A and B units are held together through C − H···π, π···π, and C-H···π(SCN) interactions, as shown in Fig. 3a. A detailed theoretical study has been done regarding the stability of the crystal packing-which is given in the later section. Only the conventional interactions along with the geometrical parameters are discussed below. The hydrogen atom, H(36), attached to a carbon atom, C(36), forms a weak hydrogen bond with a symmetry-related (− 1 + x,y,z) nitrogen atom, N(3) of a thiocyanate molecule, as shown in Fig. 3b. The details of the geometric features are given in Table 2. The hydrogen atom, H(24B), attached to a carbon

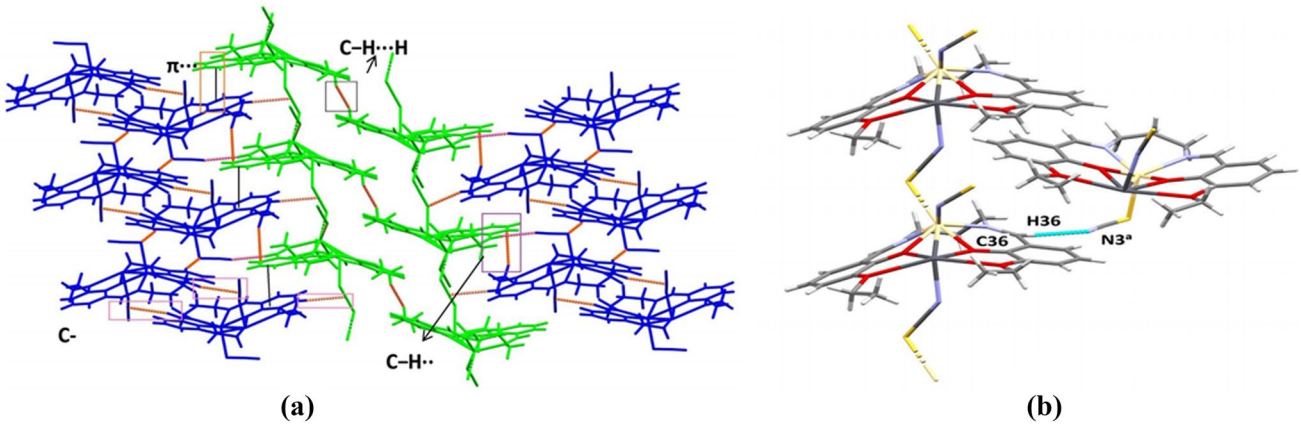

Fig. 3 **a** Crystal packing of complex **1** (represented in symmetry equivalence mode), Unit A is shown in green and unit B is shown in blue, **b** Perspective view of weak hydrogen bonding interaction in complex **1** with selective atom numbering scheme

Table 2 Hydrogen bond distances (Å) and angles (°) of the complex

D-H•••A	D-H	H•••A	D•••A	∠D-H•••A
C(36)-H(36)-N(3)[a]	0.93	2.49	3.391(12)	164

D donor, *H* hydrogen, *A* acceptor. [a] = -1 + x, y, z

atom, C(24), is involved in an inter-molecular C-H•••π interaction with a symmetry-related (1-x,-y,-z) phenyl ring C(26) – C(27) – C(28) – C(29) – C(30) – C(31) to form a supramolecular 1D structure as shown in Fig. 4a. The details of the geometric features are given in Table 3. The phenyl ring, C(37) – C(38) – C(39) – C(40) – C(41) – C(42), of complex **1** shows π···π interaction (Fig. 4b) with a phenyl ring, C(3) – C(4) – C(5) – C(6) – C(7) – C(8) with dimensions; Cg···Cg = 3.823(4) Å, α = 10.8(4)°, Cg(I) Perp = 3.614(3) Å and Cg(J) Perp = 3.547(3) Å [where α = dihedral angle

Table 3 Geometric features (distances in Å and angles in°) of the C-H···π interactions obtained in the complex

C-H···Cg (Ring)	H···Cg	C-H···Cg	C···Cg (Å)	Symmetry
C(24)-H(24B)···Cg(9)[b]	2.96	146	3.787(8)	1-x, -y, -z

Cg(9) = Centre of gravity of the ring [C(26) – C(27) – C(28) – C(29) – C(30) – C(31)].[b] = 1-x, -y,-z

Table 4 Geometric features (distances in Å and angles in°) of the π···π interactions obtained in the complex

Cg···Cg (Ring)	Cg···Cg(Å)	Cg···I (Å)	-	Cg···J (Å)
Cg(10)···Cg(17)	3.823(4)	3.614(3)		3.547(3)

Cg(10) = Centre of gravity of the ring [C(37) – C(38) – C(39) – C(40) – C(41) – C(42)]; Cg(17) = Centre of gravity of the ring [C(3) – C(4) – C(5) – C(6) – C(7) – C(8)]

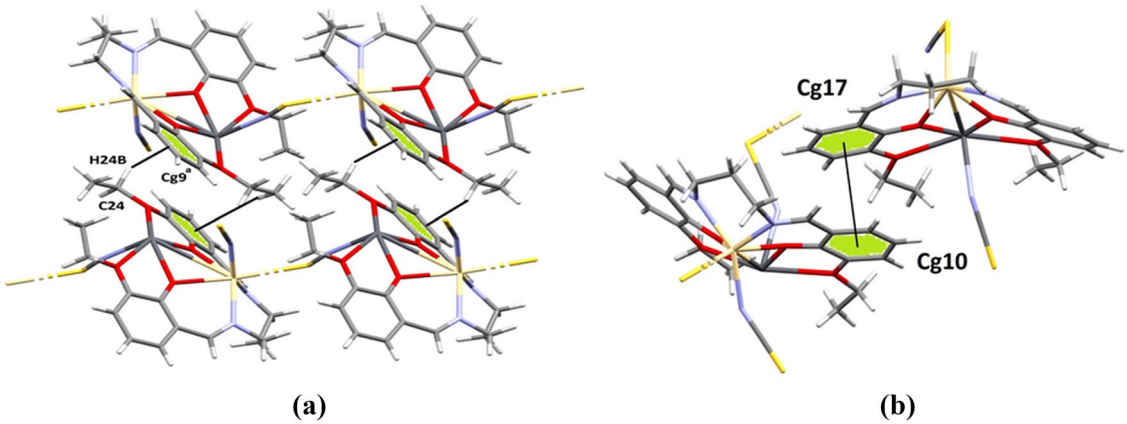

Fig. 4 **a** Perspective view of a supramolecular chain formed by C–H•••π interactions with selective atom numbering scheme, **b** Perspective view of π•••π interaction in the complex

between ring I and ring J]. The details of the geometric features are given in Table 4.

Table 5 HSA based intermolecular interactions

Entry of Intermolecular interactions	Percentage contribution
O···H	3.0 (%)
N···H	9.8 (%)
C···H	20.8 (%)
H···H	36.4 (%)
S···H	21.1 (%)
Cd···S	1.1 (%)
Pb···S	–

5 Hirshfeld Surface

The supramolecular topologies in the complex crystal structure correlate nicely with the HS mapping [118]. The hydrogen bonds were considered the possible supramolecular topologies. The molecular HS is formed based on the electron distribution and determined as the sum of spherical atom electron densities [119]. The HS is unique for a given crystal structure and spherical atomic electron densities. The HS presented here was generated using Crystal Explorer 17.5 program [120]. Equation (1), which is based on both d_e and d_i, and the van der Walls radii of the atom give the normalized contact distance (d_{norm}). Here d_e is the distance from the point to the closest nucleus external to the surface, and d_i is the distance to the nearest nucleus internal to the surface. Usually, d_{norm} displays a surface with a red, white,

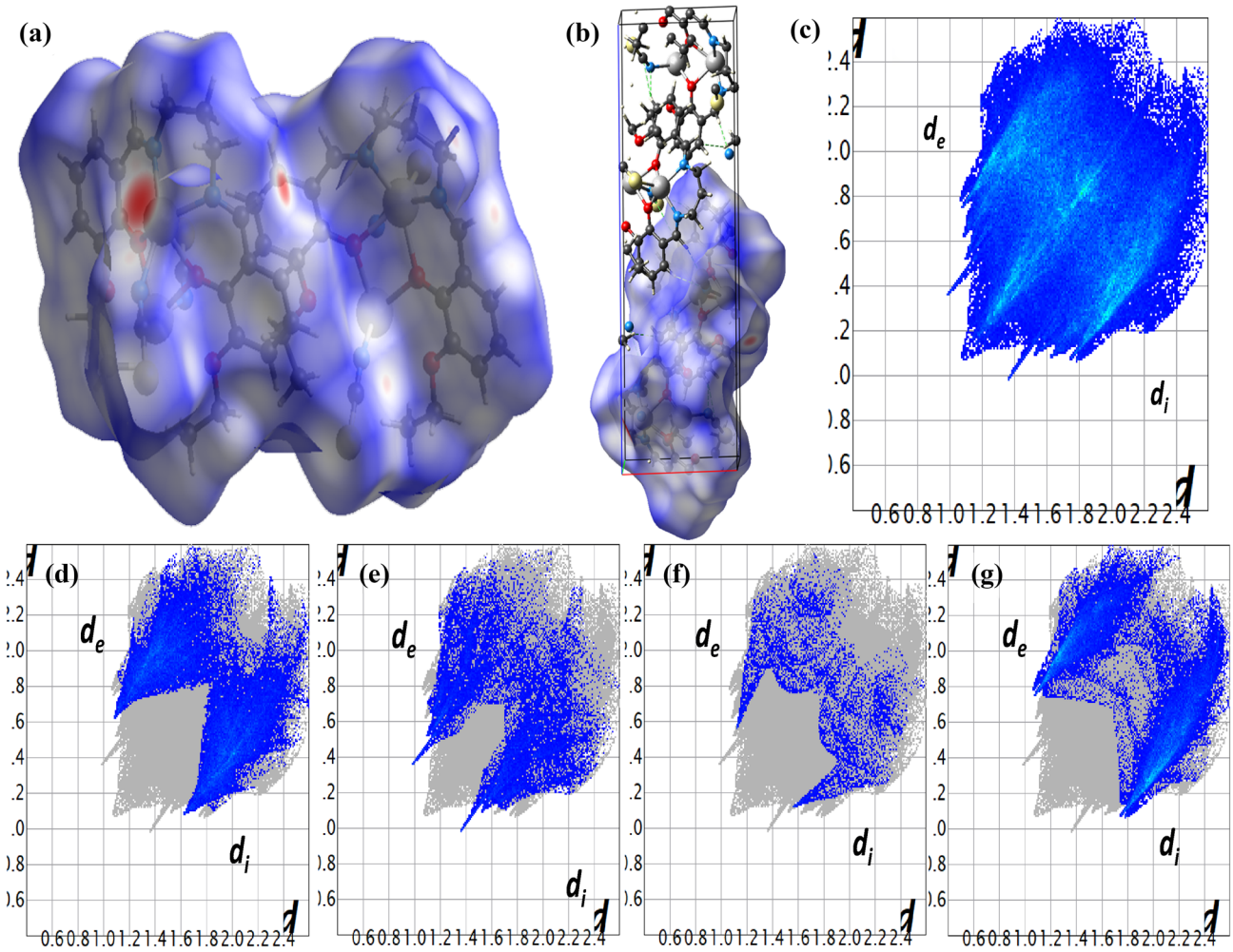

Fig. 5 **a** d_{norm} mapped on HS for visualizing the inter contacts of the complex. Colour scale in between −0.501 au (blue) and 2.463 au (red). **b** Dotted lines (in green colour) represent H-bonds. **c** Standard fingerprint plot (d_i *vs.* d_e) of the complex, **d** C···H, 20.8%, **e** N···H, 9.8%, **f** O···H, 3.0%, **g** S···H, 21.1%

and blue colour contour map, with bright red spots highlighting shorter contacts, white areas representing contacts around the van der Waals separation, and blue regions not having close connections [49]. The van der Waal interaction between the H–H is the highest among Cd···S interactions (Table 5). The 2D fingerprint plot summarizes intermolecular contacts in the complex (Fig. 5). The significant contributions in the crystal structures are H···H, C···H, and S··· H, which are responsible for supramolecular topographies in the complex. The minor contributing exchanges observed are Cd···S and O··· H.

$$d_{\text{norm}} = \frac{d_i - r_i^{\text{vdw}}}{r_i^{\text{vdw}}} + \frac{d_e - r_e^{\text{vdw}}}{r_e^{\text{vdw}}} \quad (1)$$

6 Tetrel Bonds-A Logistic approach

In the reference complex, we have first studied the different conformations adopted by the thiocyanate ions coordinated to the Cd metal center. It is different in the isolated complex (co-former B, right Fig. 6) compared to the polymeric chain (co-former A, left Fig. 6). The N-end of the SCN ligand coordinated to Cd establishes an intramolecular tetrel bond (TtB) with the Pb(II) atom in conformer B, thus influencing its final conformation. The same is not observed in conformer A because of the coordination polymer (CP) formation. It is noteworthy that TtB interactions have been previously studied in divalent Pb-atoms, demonstrating their importance in crystal engineering [105, 121, 122]. To estimate the contribution of the TtB, we have computed a theoretical model where the SCN has been rotated (right Fig. 6a–b) in such a way that the Pb···N distance becomes 5.0 Å. Consequently, the intramolecular TtB is not established in this theoretical model, and this hypothetical model is less stable than the experimental confirmation. The contribution of the tetrel bonding has been estimated as the difference between both conformations, which is – 3.06 kcal/mol, in line with previous investigations [123, 124].

7 QTAIM/NCI Plot

Figure S11 shows the combined QTAIM/NCI plot analysis (critical bond points represented as red spheres) of the discrete heteronuclear complex (co-former B). Such analysis is instrumental in revealing noncovalent interactions in real space. Also, to distinguish noncovalent, noncovalent, and coordination bonds. The reduced density gradient (RDG) surfaces obtained by the NCI Plot index analysis corroborate the existence of noncovalent interaction. It occurs in between the N-atom of the pseudohalide and the Pb atom. It is characterized by a green iso-surface, in line with the modest energy deduced from the models in Fig. 6. Interestingly, the NCI Plot index analysis also suggests that the EtO···Pb bonds are strong tetrel bonds characterized by blue RGD isosurfaces. The QTAIM analysis in Fig.S11 overlapped with the NCI Plot iso-surfaces. The tetrel bond is characterized by a bond CP and bond path (dashed bonds) connecting the N and Pb atoms. In other to corroborate the noncovalent nature of the EtO···Pb bonds, we have tabulated in Fig.S11 the values of the density ρ(r), and total energy density (Hr) at the bond CPs labeled as **a**–**c**. The positive importance of Hr at the bond CPs confirms the dominant noncovalent nature of the tetrel bonds **b** and **c**, as previously described for similar systems [125].

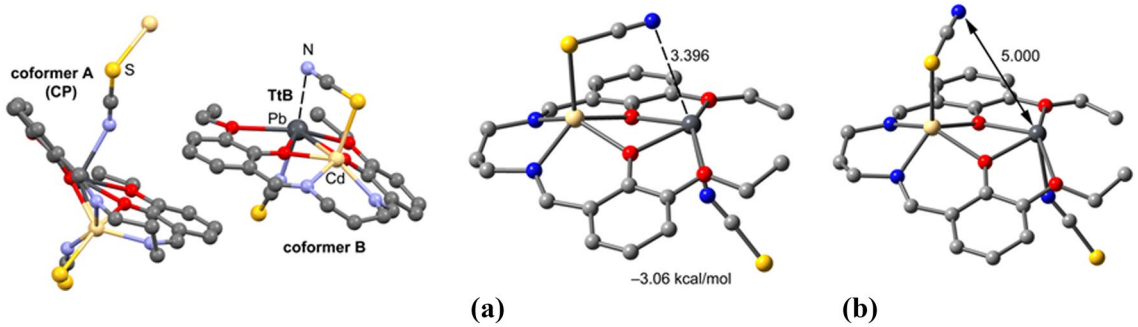

Fig. 6 (Left–Right) X-ray structure of the co-crystal with indication of both co-formers A and B. Theoretical model where the thiocyanate ligand coordinated to lead has been rotated

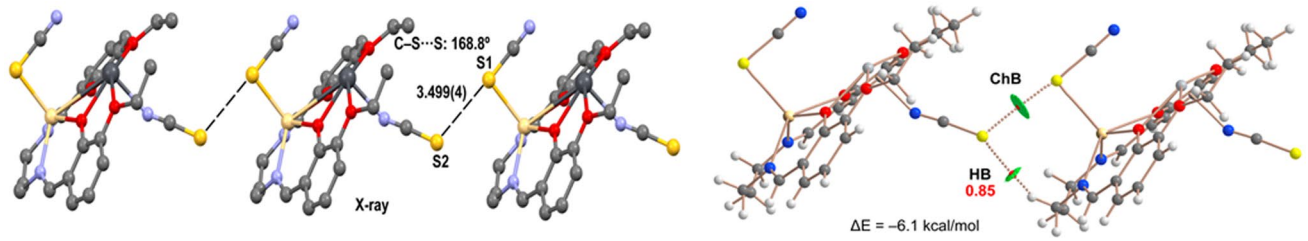

Fig. 7 (Left–Right) Partial view of the X-ray structure of the cocrystal, distance in Å (left), (Right) Combined QTAIM (bond CPs in red and bond paths as orange lines) and NCI Plot index (RDG = 0.5, ρ cut-off = 0.04 a.u., color range: $-0.04 \leq (\mathrm{sign}\lambda_2)\rho \leq 0.04$ a.u. of the dimer of co-former **B**. The HB dissociation energy is indicated in red close to the bond CP

8 Chalcogen Bonding

Figure 7 shows (left) the 1D polymeric chain observed in the solid-state of the cocrystal where the discrete [CdPb(L^1)$(SCN)_2$] co-former propagates via the formation of S···S interactions. The S-atom of the Cd-coordinated thiocyanate ligand forms a chalcogen bonding (ChB) interaction with the Cd-coordinated thiocyanate ligand. The S···S distance is 2.499(4) Å, which is shorter than the sum of the van der Waals radii ($\Sigma R_{vdw} = 3.60$ Å), and the C–S···S angle is close to linearity (168.8°) that is typical of chalcogen bonding. The QTAIM/NCI Plot analysis of a dimer extracted from the 1D supramolecular assembly discussed above (right Fig. 7). In this representation, only the intermolecular interactions are depicted. The QTAIM analysis confirms the existence of this unconventional S···S chalcogen bond, characterized by the corresponding bond CPs and bond path interconnecting both S-atoms. The green color of the NCI plot iso-surface reveals that the S···S contact is attractive, in line with the distance shorter than ΣR_{vdw}. The QTAIM/NCI Plot analysis also discloses the existence of an ancillary C–H···S bond, characterized by the bond CP, bond path and green RGD iso-surface. The dimerization energy is moderately strong ($\Delta E = -6.1$ kcal/mol) in line with the RGD iso-surface colors. To evaluate the contribution of the CH···S HB, the dissociation energy has been computed using the potential energy density value at the bond CP (V_r) and the equation proposed by Espinosa et al. ($E_{dis} = -0.5 \times V_r$) [126]. As a result, the estimated H-bond energy is only 0.85 kcal/mol, thus evidencing that the formation of the dimer is dominated by the ChB and confirming the importance of the S···S contact in the solid-state architecture of the complex.

9 MEP Surface

The MEP surface of the [CdPb(L^1)$(SCN)_2$] unit is represented in Fig. 8. It shows that the most nucleophilic part is located at the N-atom belonging to the Cd-coordinated thiocyanate (– 42 kcal/mol). The MEP is also significant

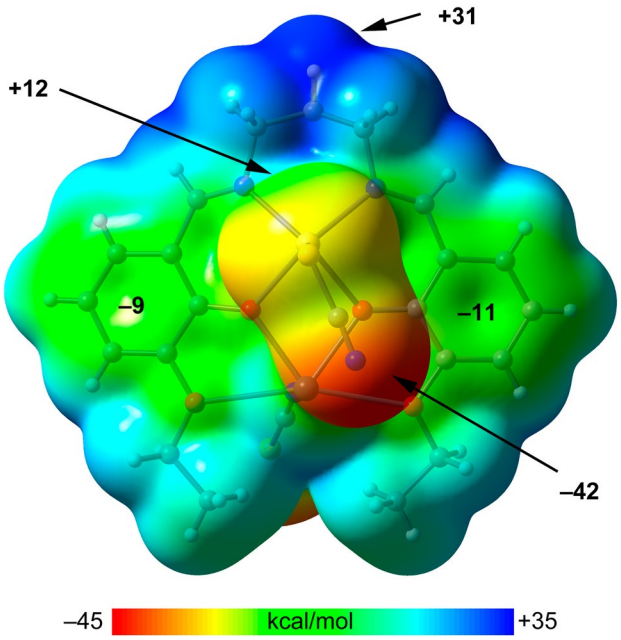

Fig. 8 MEP surface of the complex at the PBE0-D3/def2-TZVP level of theory. Iso-surface used 0.01 a.u. The MEP values at selected points of the surface are given in kcal/mol

and negative at the S-atom of the Pb-coordinated thiocyanate (not shown in Fig. 8), which is –37 kcal/mol. The MEP maximum is located at the aliphatic H-atoms of the $–(CH_2)_3–$ linker (equatorial plane). The MEP values are negative (– 9 to – 11 kcal/mol) over the aromatic rings. Interestingly, the MEP is also positive at the coordinated S-atom, thus disclosing its ability to participate in noncovalent interactions as an electron acceptor. Therefore, the S···S interaction described in Fig.S11 is electrostatically justified.

Table 6 Calculated quantum chemical parameters

E_{HOMO}	E_{LUMO}	I	A	ΔE	η	μ	χ	Pİ	ω	ε	dipole	Energy
B3LYP/LANL2DZ LEVEL												
− 5.6592	− 0.7040	5.6592	0.7040	4.9552	2.4776	0.4036	3.1816	− 3.1816	2.0428	0.4895	3.1763	− 40,396.1209
B3LYP/SDD LEVEL												
− 5.8061	− 0.8150	5.8061	0.8150	4.9912	2.4956	0.4007	3.3106	− 3.3106	2.1959	0.4554	6.9946	− 64,772.2291
HF/LANL2DZ LEVEL												
− 8.4623	2.3097	8.4623	− 2.3097	10.7720	5.3860	0.1857	3.0763	− 3.0763	0.8785	1.1383	7.1358	− 40,097.5138
HF/SDD LEVEL												
− 8.4138	1.9824	8.4138	− 1.9824	10.3962	5.1981	0.1924	3.2157	− 3.2157	0.9947	1.0053	7.6766	− 64,463.1997
M062X/LANL2DZ LEVEL												
− 6.9964	0.1317	6.9964	− 0.1317	7.1281	3.5640	0.2806	3.4323	− 3.4323	1.6527	0.6051	2.7450	− 40,376.5197
M062X/SDD LEVEL												
− 6.9920	− 0.1897	6.9920	0.1897	6.8024	3.4012	0.2940	3.5908	− 3.5908	1.8955	0.5276	2.1177	− 64,752.6859

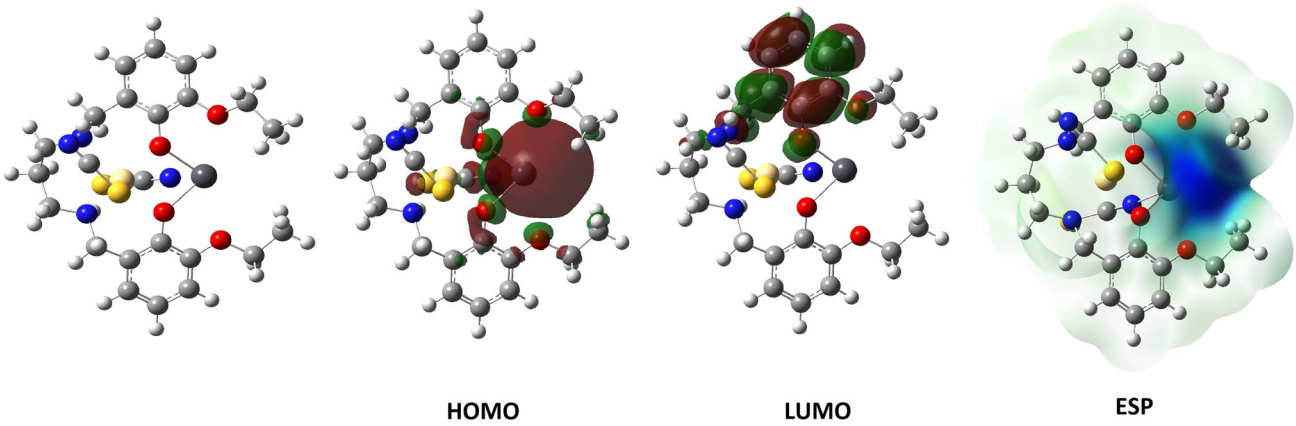

Fig. 9 HOMO–LUMO, and ESP representations of the metal complex

10 Global Reactivity Descriptors

Theoretical calculations are a fast and vital method used to compare the activities of molecules because they tell a lot of information about the active sites and activities of the molecules before experimental procedures [119]. Within the scope of this study, many quanta chemical parameters of molecules, which explain their chemical properties, are calculated with the HOMO and LUMO, two standard parameters used to describe molecule activities. The HOMO parameter, in which the most positive numerical value of this parameter has the highest activity, shows the ability of molecules to donate electrons to other molecules [127]. On the other hand, the LUMO parameter, the movement of the molecule with the most negative numerical value of this parameter, shows the ability of molecules to take electrons from other molecules [37]. These two parameters are widely used to compare the activity of molecules. All parameters calculated except these parameters are given in Table 6.

After the calculations, the visual representation of some parameters of the complex is given in Fig. 9. There are four images in this way. The first of these images shows the optimized structure, and the second and third images show which atoms the HOMO and LUMO orbitals of the molecule are located. The last picture shows the electrostatic potentials of the molecules. There are many colours in this image, from red to blue. However, the red colour is where the electron density in the molecule is highest [37]. On the other hand, the blue-coloured regions in the molecule are the places with the least electron density. The red and blue-coloured areas of the molecule have the highest activity. When the electron density is high, the molecule forms an interaction by giving electrons from this region [127]. On the other hand, areas of the molecule with low electron density accept electrons and interact. Apart from these two parameters, there are many parameters. One of them is

electronegativity, which indicates the strength of atoms in the molecule to attract bond electrons [127]. As the numerical value of this parameter increases, the molecular atoms attract the bond electrons more to themselves, thus causing the molecule's activity to decrease. However, the ΔE value of the molecules is another parameter that determines the activities. The molecule with the smallest numerical value of this parameter is considered to have the highest activity [37].

11 Non-Linear Optical (NLO) Effects

Many quanta chemical parameters are calculated when the molecules' nonlinear optical effects (NLO) are examined. The study of NLO provides essential functions such as optical modulation, frequency shifting, optical logic, optical switching, and optical memory for emerging technologies in telecommunications, signal processing, and optical interconnects [128]. The parameters are Polarizability (α) and hyperpolarizability (β), which give essential information about the molecules. These parameters have a numerical value calculated to predict the nonlinear optical properties of the materials. The dipole moment (μ) of molecules consists of two parts, Polarizability (α) and hyperpolarizability (β). NLO properties of molecules can be calculated using the parameters given below.

$$\mu = \sqrt{(\mu_x^2 + \mu_y^2 + \mu_z^2)} \tag{2}$$

$$\alpha = 2^{-1/2}[(\alpha_{xx} - \alpha_{yy})^2 + (\alpha_{yy} - \alpha_{zz})^2 + (\alpha_{zz} - \alpha_{xx})^2 + 6\alpha_{xx}^2]^{1/2} \tag{3}$$

$$\alpha = \left(\frac{\alpha_{xx} + \alpha_{yy} + \alpha_{zz}}{3}\right) \tag{4}$$

$$\beta_{tot} = [(\beta_{xxx} + \beta_{xyy} + \beta_{xzz})^2 + (\beta_{yyy} + \beta_{yzz} + \beta_{yxx})^2 + (\beta_{zzz} + \beta_{zxx} + \beta_{zyy})^2]^{1/2} \tag{5}$$

Polarizability (α_0) and hyperpolarizability (β_{tot}) values of the molecules were calculated. The unit of these values is the atomic unit (a.u.), multiplied by constant values to convert these calculated parameters into electrostatic units ($\alpha : 1a.u. = 0.148x10^{-24}esu$ and $\beta : 1a.u. = 8.639x10^{-33}esu$). It should be well known that NLO properties increase with an increasing dipole moment. Also, the linear polarizability, anisotropy of the polarizability, and first hyperpolarizability. These parameters were calculated using the HF/lanl2dz basis set for the metal complex and are in Table 7.

12 Molecular Docking/PLIP Experiments

The metal complex activity against bacteria was compared with molecular docking calculations. Crystal structures of Staphylococcus aureus protein (PDB ID: 1JIJ), pseudomonas aeruginosa protein (PDB ID: 3JPU), and Escherichia coli protein (PDB ID: 5MMN) were used for comparison. The activity of the metal complex against these proteins was calculated. The activity in which the calculations were compared with the reference molecule Streptomycin was evaluated [129]. The most critical parameter obtained in these calculations is the total energy value (E_{Total}), which is known

Table 8 Molecular docking (E_{total} energy) for complex and reference molecule

	Staphylococcus aureus	Pseudomonas aeruginosa	Escherichia coli
Complex	− 354.94	− 54.76	− 317.02
Ref. molecule	− 327.95	− 50.52	− 307.68

Table 7 NLO calculated parameters

	a. u	esu		a. u	esu
α_{xx}	357.1235	5.28543×10^{-23}	β_{xxx}	− 49.2779	− 4.258 × 10–28
α_{xy}	5.6681	8.38879×10^{-25}	β_{yyy}	− 176.7279	− 1.527 × 10–27
α_{yy}	312.1666	4.62007×10^{-23}	β_{zzz}	58.9162	5.091 × 10–28
α_{xz}	1.9470	2.88157×10^{-25}	β_{xyy}	− 95.8670	− 8.284 × 10–28
α_{yz}	45.8076	6.77952×10^{-24}	β_{xxz}	93.5867	8.087 × 10–28
α_{zz}	312.2522	4.62133×10^{-23}	β_{xxz}	− 31.9233	− 2.758 × 10–28
Δ_{α}	357.1235	5.28543×10^{-23}	β_{xzz}	125.6577	1.086 × 10–27
μ_x	− 0.5751		β_{yzz}	− 40.7410	− 3.520 × 10–28
μ_y	− 0.9183		β_{yyz}	− 97.5160	− 8.426 × 10–28
μ_z	− 0.3904		β_{total}	− 49.2779	− 4.258 × 10–28
μ_g	1.1516				

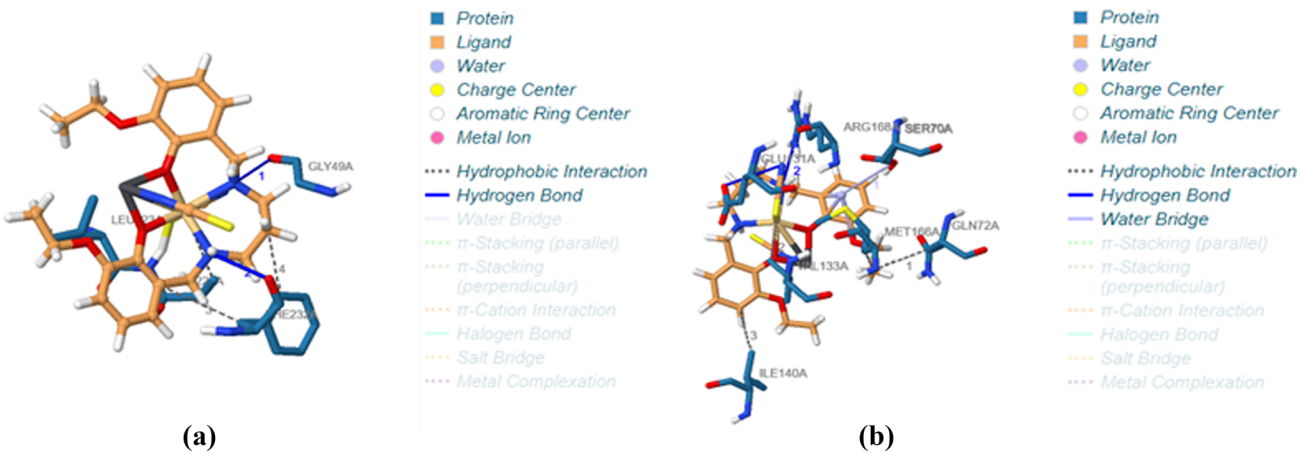

Fig. 10 **a** Representation of the interaction of the complex with staphylococcus aureus, **b** Representation of the interaction of the complex with Escherichia coli

Table 9 Hydrophobic Interactions of protein and metal complex

Index	Residue	AA	Distance	Ligand atom	Protein atom
Staphylococcus aureus—metal complex					
1	223A	LEU	3.73	3204	2151
2	224A	VAL	3.98	3199	2159
3	232A	PHE	3.80	3189	2235
4	232A	PHE	3.39	3179	2237
Escherichia coli -metal complex					
1	72A	GLN	3.50	2085	587
2	133A	VAL	3.94	2112	1039
3	140A	ILE	3.79	2108	1113
4	166A	MET	2.91	2085	1340

GLN glutamine, *ILE* isolosine, *MET* methionine, *LEU* leucine, *PHE* phenylalanine, *VAL* valine

to have the highest activity of the molecule with the most negative numerical value [130]. As a result of the calculations, the interaction of the metal complex with the proteins is given in Fig.S12. The different interaction values obtained are shown in Table 8. The most critical factor determining the activities of molecules against bacteria is the interaction between molecules and bacterial proteins. These chemical interactions are hydrogen bonds, polar and hydrophobic interactions, π-π and halogen [130]. The reference molecule used is Streptomycin. Furthermore, the PLIP (Protein–ligand interaction profiler) analysis detects chemical interactions between the metal complex and bacterial proteins. It is being investigated between which proteins these occur. It has been observed that these interactions are more intense in hydrophobic interactions and hydrogen bonding interactions. The illustration of the interactions of the bacterial protein with the metal complex is given in Figs. 10(a, b). All interactions are shown in Tables 9, 10, 11. This analysis understood no chemical interaction between the metal complex and the pseudomonas aeruginosa bacterium. Because when Fig. S12B is examined in detail, it is seen that the metal complex is too far away to form an interaction.

ructural, electronic and optical properties of 2,5-dichloro-p-xylene: experimental and theoretical. calculations using DFT method.

Table 10 Hydrogen Bonds of protein and metal complex

Index	Residue	AA	Distance H-A	Distance D-A	Donor angel	Protein donor?	Side chain	Donor Atom	Acceptor Atom
Staphylococcus aureus -metal complex									
1	49A	GLY	3.06	3.85	135.91	X	X	3166 [N_3]	460 [O_2]
2	232A	PHE	2.73	3.24	111.25	X	X	3185 [N_3]	2234 [O_2]
Escherichia coli—metal complex									
1	131A	GLU	2.92	3.44	116.29	√	√	1021 [O_3]	2127 [N_1]
2	168A	ARG	2.33	3.21	147.51	√	√	1362 [Ng^+]	2079 [N_3]

ARG Arginine, *GLU* Glutamate, *GLY* Glycine, *PHE*: Phenylalanine

Table 11 Metal complex with *Escherichia coli*

Index	Residue	AA	Dist. H-A	Dist. D-A	Donor angle	Water angle	Protein donor?	Donor atom	Acceptor atom	Water atom
1	70A	SER	2.99	3.61	134.29	73.84	√	571 [O3]	2081 [O3]	1996

SER Serine

Table 12 Mean zone diameter for the synthesized compounds

Mean zone diameter (mm)				
Microorganism	Gram-positive bacteria		Gram-negative bacteria	
	S. aureus (ATCC 25,923)	*B. subtilis (ATCC 6635)*	*P. aeruginosa* (ATCC 27,853)	*E. coli (ATCC 25,922)*
H_2L^1	15.1 ± 0.2	–	–	16.9 ± 0.04
Complex	19.67 ± 0.05	32.0 ± 0.3	35.17 ± 0.2	31.17 ± 0.2
Streptomycin	23.00 ± 0.1	30.0 ± 0.2	35.67 ± 0.1	34.83 ± 0.1
ketoconazole	–	–	–	–
DMSO	–	–	–	–

–Not detected inhibition

Table 13 MIC values of the ligand, complex and the reference drugs

Microorganism	MIC (µg/mL)	
	Gram-positive bacteria	Gram-negative bacteria
	B. subtilis (ATCC 6635)	*P. aeruginosa* (ATCC 27,853)
Complex	10.1	31.4
H_2L^1	32.7	41.5
Streptomycin	> 5	> 5

13 Antibacterial Activities

The synthesized complex and Salen ligand antimicrobial study was successfully conducted against two-gram positive and two-gram negative bacteria (Fig.S13). Mean zone diameter and MIC values of synthesized compounds were tabulated in Tables 12, 13, respectively. The complex had lower MIC (µg/mL) values than the parent Salen implying greater antimicrobial efficiencies. Salen ligand is active against Staphylococcus aureus and Escherichia coli. It means ligands don't exhibit any significant effect against Bacillus subtilis and P. aeruginosa. Also, the ligand shows good activity against Escherichia coli. The ligand of this series is an excellent antimicrobial agent against E. coli [131]. The results also explore cocrystal complex was more active against all selected microorganisms. Among them, almost the same activity against *Bacillus subtilis* compared with standard drug streptomycin but against *Pseudomonas aeruginosa, s*howed moderate-high activity. The study on *Staphylococcus aureus* and *Pseudomonas aeruginosa explores* activity lower than standard drugs. The synthesized compounds' minimum inhibitory concentration (MIC) was conducted against *Bacillus subtilis* and *Pseudomonas aeruginosa.* Interestingly, the synthesized compound shows more activity against gram-positive bacteria than gram-negative pathogens. Many literature-based complexes support the theme mentioned above [132]. It may be due to the difference in the bacterial structure features [133–135]. The in vitro antibacterial potential of the novel complex was evaluated against pathogenic bacteria and compared with the free Salen ligand. After reaching the results of MIC values of the complex and the Salen, it is possible to verify an increase in the antimicrobial activity of the complex observed after Salen ligand chelation with the metal ions [136, 137]. The complex was more active against the Gram-positive bacteria than the Gram-negative bacteria. It is probably because the cell wall of Gram-negative strains is more complex than that of Gram-positive strains. Such structural differences make the compound's entrance into the intracellular environment difficult. Consequently, it reduces the antibacterial activity of the complex [138].

13.1 Overtone's Concept

Therefore, the enhanced activity of the complex over the ligand is due to Overtone's and Tweedy's chelation concept [136, 137]. According to Overtone's idea of cell permeability and Tweedy's chelation theory, the π electron cloud delocalizes over the whole molecule due to sharing the

positive charge of the metal with the ligands. Meanwhile, the delocalization decreases the lipophobic character of the compound. Henceforth, it helps enhance penetration into the bacterial membranes and blocks metal-binding sites of microorganisms' enzymes (Fig.S14) [139]. The formation of hydrogen bonds between the complex and the cell constituents may interrupt the normal cell process. Finally, resulting in more aggressive bacterial cell death. The crucial factors are likely to be the nature of metal ions, ligand, coordinating sites, geometry, hydrophilicity, and lipophilicity. Low lipid solubility is also a significant reason for the intense action of complexes [140].

13.2 Time-kill kinetics

Time-kill kinetic study exhibits basic pharmacodynamic information on the relationship between the synthesized compound and the growth of microorganisms. The above test contributes to a better understanding of the current and future application of the complex against the diseases caused by the respective bacteria. Time kill kinetics study for cocrystal complex against all microorganisms is shown in Fig.S15, which divulges that the untreated controls in each case represented the standard growth curve against *Bacillus subtilis* and *Pseudomonas aeruginosa.* The lag period remained for one hr. After that, the exponential growth, or the log phase occurs, followed by a stationary phase. In the case of the complex microorganisms, a very short exponential growth phase was observed compared to the untreated control. The growth inhibition was observed at 5–8 h of incubation around the 8th hour of incubation when the bacterial CFU enters the declining phase, i.e., the death phase. Thus, this observation revealed that the complex shows suitable bactericidal activities.

14 Conclusions

Herein we perform a comprehensive antibacterial experimental and computational exploration for the first time, including synthetic mimics, spectroscopic findings, structural characterization, and single-crystal X-ray validation of a new (0D + 1D) Pb(II)-Salen cocrystal. The X-ray structure revealed Cd(II)/Pb(II) metal ions fulfilled trigonal-prismatic and square pyramidal geometries. The solid-state crystal architecture lavishly displayed various supramolecular interactions like H-bonding, C – H···π, π···π, C-H···π(SCN), C – H···H – C, which decisively governed the crystal packing. HSA authenticated the supramolecular interactions, and QTAIM/NCI plots observed the cocrystal's unique chalcogen ChB/tetrel bonding. The MEP surface is also significant, finding out the complex's electrophilic/nucleophilic zone. The global reactivity parameters, the HOMO–LUMO energy gap, and NLO ensure the chemical reactivity and the sensitive optical behaviour. The complex and ligand were screened in vitro against two-gram + ve and two-gram -ve bacterial strains. The result showed complex has significantly higher antibacterial activity than the parent ligand. MD/PLIP experiments were performed to examine the interaction of the metal complex with bacterial proteins based on the total energy against the reference molecule streptomycin. These two computational profiles explore the complex biological effectiveness. The time-kill kinetics bring forth the cocrystal bactericidal activities. The outcomes of MD/PLIP will be an essential guide for future in vitro and in vivo studies. This work concludes that the synthesized cocrystal could be used as an antibacterial agent. Finally, DFT results could interest theoreticians and scientists, especially in crystal engineering and supramolecular chemistry.

15 Supplementary information

CCDC 2,053,004 contains the supplementary crystallographic data for cocrystal **1**.These data can be obtained free of charge via http://www.ccdc.cam.ac.uk/conts/retrieving.html, or from the Cambridge Crystallographic Data Centre, 12 Union Road, Cambridge CB2 1EZ, UK; fax: (+44) 1223–336-033; or e-mail: deposit@ccdc.cam.ac.uk.

Supplementary Information The online version contains supplementary material available at https://doi.org/10.1007/s10904-022-02448-0.

Acknowledgements This research has not received specific funding from any funding agency in public, commercial or not-for-profit sectors. All authors thank the Central Laboratory of Tamralipta Mahavidyalaya, Tamluk, West Bengal, India, funded by the DST-FIST Project (Level-0) under the Department of Science and Technology, Govt. from India. The corresponding author Dhrubajyoti Majumdar thanks Dr. Abdul Motin, principal of Tamralipta Mahavidyalaya, for providing the sophisticated research laboratory.

Author contributions DJM: was the project administrator and conceived the whole research idea, performed data curation, conceptualization, methodology, research investigation, software visualization, writing review, total draft preparation, and editing. JEP: collected the experimental data of the antibacterial study. AF, RMG, and BT: have performed DFT-based experiments. SR and KB: were involved in X-ray structure analysis of single crystals and various Graphics preparations. All manuscript authors carefully read and approved the final version before submission.

Declarations

Conflict of interest The authors declare no competing interest or personal relationships that could have appeared to impact the work reported in this paper.

References

1. L.K. Das, A. Biswas, Carlos, J. Gomez-Garcia, M.G.B. Drew, Inorg. Chem. **53**(1), 434–445 (2014)
2. R. Golbedaghi, R. Fausto, Polyhedron **155**, 1–12 (2018)
3. S. Zinatloo-Ajabshira, M.S. Morassaeib, M. Salavati-Niasari, Compos. B **167**, 643–653 (2019)
4. S.A. Heidari-Asil, S. Zinatloo-Ajabshir, H.A. Alshamsi, A. Al-Nayili, Q.A. Yousif, M. Salavati-Niasari **47**, 16852–16861 (2022)
5. S. Zinatloo-Ajabshir, M. Emsaki, G. Hosseinzadeh, J Colloid Interface Sci. **619**, 1–13 (2022)
6. A. Zonarsaghar, M. Mousavi-Kamazani, S. Zinatloo-Ajabshir, J Mater Sci **33**, 6549–6554 (2022)
7. K. Mahdavi, S. Zinatloo-Ajabshir, Q.A. Yousif, M. Salavati-Niasari, Ultrason Sonochem. **82**, 105892 (2022)
8. S.M. Tabatabaeinejad, S. Zinatloo-Ajabshir, O. Amiri, M. Salavati-Niasari, RSC Adv. **11**, 40100–40111 (2021)
9. S.L. Childs, M.J. Zaworotko, Cryst. Growth Des. **9**, 4208–4421 (2009)
10. J. I. Arenas-Garca, D. Herrera-Ruiz, K. Mondragon-Vasquez, H. Morales-Rojas, H. Höpfl, Cryst. Growth Des. **12,** 811−824 (2012)
11. C. Puigjaner, R. Barbas, A. Portell, I. Valverde, X. Vila, X. Alcob, M. Font-Bardia, R. Prohens, CrystEngComm **14**, 362–365 (2012)
12. J. Bernstein, Cryst. Growth Des. **11**, 632–650 (2011)
13. C.B. Aakeroy, N.R. Champness, C. Janiak, CrystEngComm **12**, 22–43 (2010)
14. R. Bishop, Acc. Chem. Res. **42**, 67–78 (2009)
15. A. Nangia, J. Chem. Sci. **122**, 295–310 (2010)
16. M. Habgood, S.L. Price, Cryst. Growth Des. **10**, 3263–3272 (2010)
17. B. Moulton, M.J. Zaworotko, Chem. Rev. **101**, 1629–1658 (2001)
18. G.P. Stahly, Cryst. Growth Des. **7**, 1007–1026 (2007)
19. G. R. Desiraju, Angew. Chem., Int. Ed. **46,** 8342−8356 (2007)
20. S. Benmansour, M. Marchivie, S. Triki, C.J. Gómez-García, Crystals **2**, 306–326 (2012)
21. M. Nayek, A. Jana, M. Fleck, S. Hazra, S. Mohanta, CrystEngComm **12**, 1416–1421 (2010)
22. C.C. Chou, C.C. Su, H.L. Tsai, K.H. Lii, Inorg. Chem. **44**, 628–632 (2005)
23. E.A. Buvaylo, V.N. Kokozay, K. Rubini, O.Y. Vassilyeva, B.W. Skelton, J. Mol. Struct. **1072**, 129–136 (2014)
24. R. Golbedaghi, S. Salehzadeh, H. Khavasi, A.G. Blackman, Polyhedron **68**, 151–156 (2014)
25. W. Purcell, S.S. Basson, J.G. Leipoldt, A. Roodt, H. Preston, Inorg. Chim. Acta. **234**, 153–156 (1995)
26. A. Jana, S. Mohanta, CrystEngComm **16**, 5494–5515 (2014)
27. A. Jana, R. Koner, M. Nayak, P. Lemoine, S. Dutta, M. Ghosh, S. Mohanta, Inorg. Chim. Acta. **365**, 71–77 (2011)
28. S. Bhattacharya, A. Jana, S. Mohanta, Polyhedron **62**, 234–242 (2013)
29. S. Pal, A.K. Nandi, Macromolecules **36**, 8426–8432 (2003)
30. P. Shukla, R. K. Metre, M.-H. Du, X.-J. Kong, S. Das, Eur. J. Inorg. Chem. 2216–2223 (2019)
31. S. Basavoju, D. Boström, S. Velaga, Pharm. Res. **25**, 530–541 (2008)
32. N.E. Eltayeb, S.G. Teoh, S. Chantrapromma, H.K. Fun, R. Adnan, Acta Cryst. E **64**, m626–m627 (2008)
33. M. Nayak, S. Hazra, P. Lemoine, R. Koner, C.R. Lucas, S. Mohanta, Polyhedron **27**, 1201–1213 (2008)
34. S. Karki, T. Friščić, L. Fábián, P.R. Laity, G.M. Day, W. Jones, Adv. Mater. **21**, 3905–3909 (2009)
35. J. Wouters, S. Rome, L. Quere, RSC Drug Discov. 338–382 (2011)
36. N. Blagden, S.J. Colesb, D.J. Berry, CrystEngComm **16**, 5753–5761 (2014)
37. D.J. Majumdar, B. Tüzün, T.K. Pal, V. Reena, Saini, K. Bankura, D. Mishra, Polyhedron **210**, 115504 (2021)
38. D.J. Majumdar, T.K. Pal, S.A. Sakib, S. Das, K. Bankura, D. Mishra, Inorg. Chem. Comm. **128**, 108609 (2021)
39. S.M. Woodley, R. Catlow, Nature Mat. **7**, 937–946 (2008)
40. A.R. Oganov (ed.), *Modern Methods of Crystal Structure Prediction* (Wiley-VCH Verlag GmbH Co. KGaA, Weinheim, Germany, 2011)
41. A. Hazari, L.K. Das, A. Bauza, A. Frontera, A. Ghosh, Dalton Trans. **43**, 8007–8015 (2014)
42. D.J. Majumdar, Y. Agrawal, R. Thomas, Z. Ullah, M.K. Santra, S. Das, T.K. Pal, K. Bankura, D. Mishra, Appl. Organomet. Chem. **34**, e5269 (2019)
43. J.S. Murray, P. Lane, P. Politzer, J. Mol. Model. **15**, 723–729 (2009)
44. J.S. Murray, K.E. Riley, P. Politzer, T. Clark, Aust. J. Chem. **63**, 1598–1607 (2010)
45. P. Politzer, J.S. Murray, T. Clark, Phys. Chem. Chem. Phys. **15**, 11178–11189 (2013)
46. A. Bauzá, T.J. Mooibroek, A. Frontera, Chem. Phys. Chem. **16**, 2496–2517 (2015)
47. A. Bauzá, T.J. Mooibroek, A. Frontera, Angew. Chem. Int. Ed. **52**, 12317–12321 (2013)
48. S.J. Grabowski, Phys. Chem. Chem. Phys. **16**, 1824–1834 (2014)
49. S. Thakur, Rosa M. Gomila, A. Frontera, S. Chattopadhyay, Cryst. Eng. Comm. **23,** 5087 (2021)
50. D.J. Majumdar, J.K. Biswas, M. Mondal, M.S. Babu, S. Das, R.K. Metre, S.S. SreeKumar, K. Bankura, D. Mishra, ChemistrySelect **3**, 2912–2925 (2018)
51. D. J. Majumdar, M. S. Surendra Babu, S. Das, C. Mohapatra, J. K. Biswas, M. Mondal, Chem. Select **2,** 4811–4822 (2017)
52. D.J. Majumdar, S. Das, J.K. Biswas, M. Mondal, J. Mol. Struct. **1134**, 617–624 (2017)
53. D.J. Majumdar, S. Dey, S.S. Sreekumar, S. Das, D. Das, R.K. Metre, K. Bankura, D. Mishra, Chem. Sel. **3**, 12371–12382 (2018)
54. D.L. Reger, T.D. Wright, C.A. Little, J.J.S. Lamba, M.D. Smith, Inorg. Chem. **40**, 3810–3814 (2001)
55. H. Fleischer, D. Schollmeyer, Inorg. Chem. **43**, 5529–5536 (2004)
56. A. Morsali, A.R. Mahjoub, Helv. Chim. Acta. **87**, 2717–2722 (2004)
57. J. Parr, Polyhedron **16**, 551–566 (1997)
58. A. Olvera, G. Shi, H. Djieutedjeu, A. Page, C. Uher, E. Kioupakis, P.F.P. Poudeu, Inorg. Chem. **54**, 746–755 (2015)
59. C.A. Randall, A.S. Bhalla, T.R. Shrout, L.E. Cross, J. Mater. Res. **5**, 829–834 (1990)
60. F. Cheng, J. Liang, Z. Tao, J. Chen, Adv. Mater. **23**, 1695–1715 (2011)
61. L. Zhang, Y.-Y. Qin, Z.-J. Li, Q.-P. Lin, J.-K. Cheng, J. Zhang, Y.-G. Yao, Inorg. Chem. **47**, 8286–8293 (2008)
62. Y. Cheng, T.J. Emge, J.G. Brennan, Inorg. Chem. **35**, 342–346 (1996)
63. R.L. Davidovich, V. Stavila, D.V. Marinin, E.I. Voit, K.H. Whitmire, Coord. Chem. Rev. **253**, 1316–1352 (2009)
64. G. Mahmoudi, A. Bauzá, A. Frontera, Dalton Trans. **45**, 4965–4969 (2016)
65. M.S. Gargari, V. Stilinović, A. Bauzá, A. Frontera, P. McArdle, D.V. Derveer, S.W. Ng, G. Mahmoudi, Chem. Eur. J. **21**, 17951–17958 (2015)
66. C. Gourlaouen, O. Parisel, H. Gérard, Dalton Trans. **40**, 11282–11288 (2011)

67. S. Mirdya, S. Roy, S. Chatterjee, A. Bauza, A. Frontera, S. Chattopadhyay, Cryst. Growth Des. DOI: https://doi.org/10.1021/acs.cgd.9b00881.
68. G. Mahmoudi, A. Bauzá, M. Amini, E. Molins, J.T. Magued, A. Frontera, Dalton Trans. **45**, 10708–10716 (2016)
69. A. Bauza, T.J. Mooibroek, A. Frontera, Chem. Rec. **16**, 473–487 (2016)
70. M.S. Gargari, V. Stilinović, A. Bauzá, A. Frontera, P. McArdle, D.V. Van Derveer, S.W. Ng, G. Mahmoudi, Chem. - Eur. J. **21**, 17951–17958 (2015)
71. G. Mahmoudi, E. Zangrando, M.P. Mitoraj, A.V. Gurbanov, F.I. Zubkov, M. Moosavifar, I.A. Konyaeva, A.M. Kirillov, D.A. Safin, New J. Chem. **42**, 4959–4971 (2018)
72. S.J. Grabowski, Appl. Organomet. Chem. **31**, e3727 (2017)
73. G. M. Sheldrick, SADABS, a software for empirical absorption correction, Ver.2.05; University of Göttingen: Göttingen, Germany, (2002)
74. SMART & SAINT Software Reference manuals Version 6.45; Bruker Analytical X-ray Systems, Inc.: Madison, WI, (2003)
75. SHELXTL Reference Manual Ver. 6.1; Bruker Analytical X-ray Systems, Inc.: Madison, WI, (2000)
76. G. M. Sheldrick, SHELXTL, a software for empirical absorption correction Ver.6.12; Bruker AXS Inc.: WI. Madison, (2001)
77. O.V. Dolomanov, L.J. Bourhis, R.J. Gildea, J.A.K. Howard, H. Puschmann, OLEX2, *OLEX2*: a complete structure solution, refinement, and analysis program. J. Appl. Crystallog. **42**, 339–341 (2009)
78. Gaussian 16, Revision C.01, M. J. Frisch, G. W. Trucks, H. B. Schlegel, G. E. Scuseria, M. A. Robb, J. R. Cheeseman, G. Scalmani, V. Barone, G. A. Petersson, H. Nakatsuji, X. Li, M. Caricato, A. V. Marenich, J. Bloino, B. G. Janesko, R. Gomperts, B. Mennucci, H. P. Hratchian, J. V. Ortiz, A. F. Izmaylov, J. L. Sonnenberg, D. Williams-Young, F. Ding, F. Lipparini, F. Egidi, J. Goings, B. Peng, A. Petrone, T. Henderson, D. Ranasinghe, V. G. Zakrzewski, J. Gao, N. Rega, G. Zheng, W. Liang, M. Hada, M. Ehara, K. Toyota, R. Fukuda, J. Hasegawa, M. Ishida, T. Nakajima, Y. Honda, O. Kitao, H. Nakai, T. Vreven, K. Throssell, J. A. Montgomery, Jr., J. E. Peralta, F. Ogliaro, M. J. Bearpark, J. J. Heyd, E. N. Brothers, K. N. Kudin, V. N. Staroverov, T. A. Keith, R. Kobayashi, J. Normand, K. Raghavachari, A. P. Rendell, J. C. Burant, S. S. Iyengar, J. Tomasi, M. Cossi, J. M. Millam, M. Klene, C. Adamo, R. Cammi, J. W. Ochterski, R. L. Martin, K. Morokuma, O. Farkas, J. B. Foresman, D. J. Fox, Gaussian, Inc., Wallingford CT, (2016)
79. S. Grimme, J. Antony, S. Ehrlich, H. Krieg, J. Chem. Phys. **132**, 154104 (2010)
80. F. Weigend, R. Ahlrichs, Phys. Chem. Chem. Phys. **7**, 3297–3305 (2005)
81. F. Weigend, Phys. Chem. Chem. Phys. **8**, 1057–1065 (2006)
82. M. Karmakar, A. Frontera, S. Chattopadhyay, T.J. Mooibroek, A. Bauzá, Int. J. Mol. Sci. **21**, 7091 (2020)
83. N.S. Soldatova, P.S. Postnikov, V.V. Suslonov, T.Y. Kissler, D.M. Ivanov, M.S. Yusubov, B. Galmés, A. Frontera, V.Y. Kukushkin, Org. Chem. Front. **7**, 2230–2242 (2020)
84. R.F.W. Bader, Chem. Rev. **91**, 893–928 (1991)
85. J. Contreras-García, E.R. Johnson, S. Keinan, R. Chaudret, J.-P. Piquemal, D.N. Beratan, W. Yang, J. Chem. Theory Comput. **7**, 625–632 (2011)
86. T. A. Keith, AIM All (Version 13.05.06), TK Gristmill Software, Overland Park, KS, (2013)
87. M. Rbaa, S. Haida, B. Tuzun, A. El Hassane, A. Kribii, Y. Lakhrissi, E. Berdimurodov, J. Mol. Struct.132688 (2022)
88. Y. Lakhrissi, M. Rbaa, B. Tuzun, A. Hichar, K. Ounine, F. Almalki, B. Lakhrissi, J. Mol. Struct.132683 (2022)
89. E. H. Alici, A. T. Bilgiçli, B. Tüzün, A. Günsel, G. Arabaci, M. N. Yarasir, J. Mol. Struct. 132634 (2022)
90. I. A. S. Al-Janabi, S. C. Yavuz, S. Köprü, M. Tapera, H. Kekeçmuhammed, S. Akkoç, E. Sarıpınar, J. Mol. Struct. 132627 (2022)
91. A.D. Becke, J. Chem. Phys. **96**(3), 2155–2160 (1992)
92. D. Vautherin, D.T. Brink, Phys. Rev. C **5**(3), 626 (1972)
93. E.G. Hohenstein, S.T. Chill, C.D. Sherrill, J. Chem. Theory Comput. **4**(12), 1996–2000 (2008)
94. X. Qiu, C.A. Janson, W.W. Smith, S.M. Green, P. McDevitt, K. Johanson, R.L. Jarvest, Protein Sci. **10**(10), 2008–2016 (2001)
95. R. Dennington, T. A. Keith, J. M. Millam, GaussView 6.0. 16. Semichem Inc.: Shawnee Mission, KS, USA, (2016)
96. M. A. Bhat, B. TÜZÜN, N. A. Alsaif, A. A. Khan, A. M. Naglah, J. Mol. Struct. 132600 (2022)
97. M. Rezaeivala, S. Karimi, K. Sayin, B. Tüzün, Colloids and surfaces a: physicochemical and engineering aspects 128538 (2022)
98. D. Ritchie, T. Orpailleur, Hex 8.0. 0 User Manual. Protein Docking Using Spherical Polar Fourier Correlations Copyright C (2013)
99. Y. Zou, S.K. Nair, Chem. Biol. **16**(9), 961–970 (2009)
100. P. Panchaud, T. Bruyere, A.C. Blumstein, D. Bur, A. Chambovey, E.A. Ertel, G. Rueedi, J. Med. Chem. **60**(9), 3755–3775 (2017)
101. M.F. Adasme, K.L. Linnemann, S.N. Bolz, F. Kaiser, S. Salentin, V.J. Haupt, M. Schroeder, Nucleic Acids Res. **49**(W1), W530–W534 (2021)
102. S. Roy, M.G.B. Drew, A. Bauza´, A. Frontera, S. Chattopadhyay, New J. Chem. **42**, 6062–6076 (2018)
103. M. Dolai, T. Mistri, A. Panja, M. Ali, Inorg. Chim. Acta. **399**, 95–104 (2013)
104. S. Mirdya, S. Banerjee, S. Chattopadhayay, CrystEngComm **22**, 237–247 (2020)
105. S. Mirdya, S. Roy, S. Chatterjee, A. Bauzá, A. Frontera, S. Chattopadhyay, Cryst. Growth Des. **19**, 5869–5881 (2019)
106. S. Mirdya, A. Frontera, S. Chattopadhayay, CrystEngComm **21**, 6859–6868 (2019)
107. M. Maiti, S. Thakurta, D. Sadhukhan, G. Pilet, G.M. Rosair, A. Nonat, L.J. Charbonniere, S. Mitra, Polyhedron **65**, 6–15 (2013)
108. A.B.P. Lever, *Inorganic Spectroscopy*, 2nd edn. (Elsevier, New York, 1984)
109. L.K. Das, M.G.B. Drew, A. Ghosh, Inorg. Chim. Acta. **394**, 247–254 (2013)
110. D.K. Mishra, U.K. Singha, A. Das, S. Dutta, P. Kar, A. Chakraborty, A. Sen, B. Sinha, J. Coord. Chem. **71**, 2165–2182 (2018)
111. D. Sadhukhan, A. Ray, G. Rosair, L. Charbonnière, S. Mitra, BCSJ **84**, 211–217 (2011)
112. M. Amirnasr, K.J. Schenk, M. Salavati, S. Dehghanpour, A. Taeb, A. Tadjarodi, J. Coord. Chem. **56**, 231–243 (2003)
113. S. M. Sheta, M. A. Akl, H. E. Saad, El-Sayed R. H. El-Gharkawy, RSC Adv. **10,** 5853–5863 (2020)
114. A.W. Addison, N.T. Rao, J. Reedijk, J. van Rijn, G.C. Verschoor, J. Chem. Soc. Dalton Trans. **7**, 1349–1356 (1984)
115. D. Cremer, J.A. Pople, J. Am. Chem. Soc. **97**, 1354–1358 (1975)
116. S. Roy, K. Harms, S. Chattopadhyay, Polyhedron **91**, 10–17 (2015)
117. S. Roy, M.G.B. Drew, A. Bauzá, A. Frontera, S. Chattopadhyay, Dalton Trans. **46**, 5384–5397 (2017)
118. J.J. McKinnon, M.A. Spackman, A.S. Mitchell, Acta Crystallogr. Sect. B **60**, 627–668 (2004)
119. D.J. Majumdar, B. Tüzün, T.K. Pal, S. Das, Kalipada Bankura. J. Inorg. Organomet. Polym. **32**, 1159–1176 (2022)
120. C. F. Mackenzie, P. R. Spackman, D. Jayatilaka, M. A. packman, IUCrJ **4(5),** 575–587 (2017)

121. I. García-Santos, A. Castiñeiras, G. Mahmoudi, M. G. Babashkina, E. Zangrando, Rosa M. Gomila, A. Frontera, D. A. Safin, Crystengcomm. **24,** 368–378 (2022)
122. G. Mahmoudi, S. k. Seth, A. Bauza, F. I. Zubkov, A. Frontera, Crystals **10,** 568 (2020)
123. G. Mahmoudi, M. Abedi, S.E. Lawrence, E. Zangrando, M.G. Babashkina, A. Klein, A. Frontera, D.A. Safin, Molecules **25**(18), 4056 (2020)
124. G. Mahmoudi, A. Masoudiasl, F.A. Afkhami, J.M. White, E. Zangrando, A.V. Gurbanov, A. Frontera, D.A. Safin, J. Mol. Struct. **1234**, 130139 (2021)
125. F.A. Afkhami, G. Mahmoudi, F. Qu, A. Gupta, E. Zangrando, A. Frontera, D.A. Safin, Inorg. Chim. Acta. **502**, 119350 (2020)
126. E. Espinosa, E. Molins, C. Lecomte, Chem. Phys. Lett. **285**, 170–173 (1998)
127. Z. Kökbudak, S. Akkoç, H. Karataş, B. Tüzün, G. Aslan, ChemistrySelect **7**(3), e202103679 (2022)
128. A. Üngördü, K. Sayin, Chem. Phys. Lett. **733**, 136677 (2019)
129. D. Kısa, N. Korkmaz, P. Taslimi, B. Tuzun, S. Tekin, A. Karadag, F. Şen, Bioorg. Chem. **101**, 104066 (2020)
130. U. M. Koçyiğit, P. Taslimi, B. Tüzün, H. Yakan, H. Muğlu, E. Güzel, J. Biomol. Struct. Dyn. 1–11 (2020)
131. D. J. Majumdar, Swapan Dey, S. S. Sreejith, J. K. Biswas, M. Mondal, P. Shukla, S. Das, T. K. Pal, D. Das, K. Bankura, D. Mishra, J. Mol. Struct. **1179**, 694–708 (2019)
132. W. A. Siddiqui1, M. Khalid, A. Ashraf, I. Shafiq, M. Parvez, M. Imran, A. Irfan, M. Hanif, M. U. Khan, F. Sher, A. Ali, Appl. Organomet. Chem. e6464 (2021)
133. V. Pehlivan, E. Biçer, Y.G. Bekiroglu, N. Dege, Int. J. Electrochem. Sci. **13**, 10733 (2018)
134. X. Ran, L. Wang, D. Cao, Y. Lin, J. Hao, Appl. Organomet. Chem. **25**, 9 (2011)
135. G.B. Bagihalli, S.A. Patil, J. Coord. Chem. **62**, 1690 (2009)
136. H. Sakurai, Y. Kojima, Y. Yoshikawa, K. Kawabe, H. Yasui, Coord. Chem. Rev. **226**, 187 (2002)
137. N.U.H. Khan, K.S.H. Nadeem, Middle east. J. Sci. Res. **16**, 1109 (2013)
138. T. J. Beveridge, Ultrastructure, chemistry, and function of the bacterial wall, in International Review of Cytology, (Eds: G. H. Bourne, J. F. Danielli, K. W. Jeon), Academic Press 229 (1981)
139. M.A. Malik, O.A. Dar, P. Gull, M.Y. Wani, A.D. Hashmi, Med. Chem. Commun. **9**, 409–436 (2018)
140. D.J. Majumdar, D. Das, S. Nag, M. Bhattacharyya, D.K. Singh, D. Parai, K. Bankura, D. Mishra, J. Mol. Struct. **1222**, 128951 (2020)

Publisher's Note Springer Nature remains neutral with regard to jurisdictional claims in published maps and institutional affiliations.